Computers in Biology and Medicine 166 (2023) 107543



Contents lists available at ScienceDirect

Computers in Biology and Medicine

journal homepage: www.elsevier.com/locate/compbiomed



MRI-based parameter inference for cerebral perfusion modelling in health and ischaemic stroke

T.I. Józsa [a,*,1], J. Petr [b,c], S.J. Payne [d,e], H.J.M.M. Mutsaerts [c]

[a] Centre for Computational Engineering Sciences, School of Aerospace, Transport and Manufacturing, Cranfield University, Cranfield, UK
[b] Helmholtz-Zentrum Dresden-Rossendorf, Institute of Radiopharmaceutical Cancer Research, Dresden, Germany
[c] Department of Radiology and Nuclear Medicine, Amsterdam Neuroscience, Amsterdam University Medical Centers, Location VUmc, Amsterdam, The Netherlands
[d] Institute of Biomedical Engineering, Department of Engineering Science, University of Oxford, Oxford, UK
[e] Institute of Applied Mechanics, National Taiwan University, Taipei, Taiwan

ARTICLE INFO

Keywords:
Cerebral blood flow
Acute ischaemic stroke
Magnetic resonance imaging
Computational modelling

ABSTRACT

Cerebral perfusion modelling is a promising tool to predict the impact of acute ischaemic stroke treatments on the spatial distribution of cerebral blood flow (CBF) in the human brain. To estimate treatment efficacy based on CBF, perfusion simulations need to become suitable for group-level investigations and thus account for physiological variability between individuals. However, computational perfusion modelling to date has been restricted to a few patient-specific cases. This study set out to establish automated parameter inference for perfusion modelling based on neuroimaging data and thus enable CBF simulations of groups. Magnetic resonance imaging (MRI) data from 75 healthy senior adults were utilised. Brain geometries were computed from healthy reference subjects' T1-weighted MRI. Haemodynamic model parameters were determined from spatial CBF maps measured by arterial spin labelling (ASL) perfusion MRI. Thereafter, perfusion simulations were conducted in 75 healthy cases followed by 150 acute ischaemic stroke cases representing an occlusion and CBF cessation in the left and right middle cerebral arteries. The anatomical fitness of the brain geometries was evaluated by comparing the simulated grey (GM) and white matter (WM) volumes to measurements in healthy reference subjects. Strong positive correlations were found in both tissue types (GM: Pearson's r 0.74, $P < 0.001$; WM: Pearson's r 0.84, $P < 0.001$). Haemodynamic parameter tuning was verified by comparing the total volumetric blood flow rate to the brain in healthy reference subjects and simulations (Pearson's r 0.89, $P < 0.001$). In acute ischaemic stroke cases, the simulated infarct volume using a perfusion-based estimate was 197 ± 25 ml. Computational predictions were in agreement with anatomical and haemodynamic values from the literature concerning T1-weighted, T2-weighted, and phase-contrast MRI measurements in healthy scenarios and acute ischaemic stroke cases. The acute stroke simulations did not capture small infarcts (left tail of the distribution), which could be explained by neglected compensatory mechanisms, e.g. collaterals. The proposed parameter inference method provides a foundation for group-level CBF simulations and for *in silico* clinical stroke trials which could assist in medical device and drug development.

1. Introduction

Acute ischaemic strokes (AIS) are caused by occlusions of major cerebral arteries and account for the majority of stroke cases [1,2]. Thrombolysis [2] and thrombectomy [1] revolutionised stroke treatment but more than 60% of patients remain functionally dependent or die [3,4]. The *IN Silico* clinical trials for the treatment of acute Ischaemic STroke (INSIST) consortium [5,6] set out to improve existing stroke treatments based on simulations. The proposed computational models capture the key processes involved in AIS treatments, such as clot resolution by a thrombolytic drug [7,8], clot removal with a stent retriever [9,10], and the development of micro-occlusions due to clot fragmentation [11]. In AIS, perfusion shortage is the primary driver of infarct formation associated with irreversible brain tissue and function loss. Therefore, one of the models proposed in INSIST simulates pre-treatment and post-treatment spatial perfusion distributions [12,13].

* Corresponding author at: Centre for Computational Engineering Sciences, School of Aerospace, Transport and Manufacturing, Cranfield University, Cranfield, UK.
E-mail address: jozsait@gmail.com (T.I. Józsa).
[1] tamas[DOT]jozsa[AT]cranfield[DOT]ac[DOT]uk

https://doi.org/10.1016/j.compbiomed.2023.107543
Received 7 March 2023; Received in revised form 7 September 2023; Accepted 28 September 2023
Available online 30 September 2023
0010-4825/© 2023 The Authors. Published by Elsevier Ltd. This is an open access article under the CC BY license (http://creativecommons.org/licenses/by/4.0/).

Thereafter, the efficacy of various treatment strategies, such as combined thrombolysis and thrombectomy against sole thrombectomy, can be estimated based on perfusion modelling. The fundamental assumption is that a large and temporally sustained perfusion drop compared to a healthy reference state predicts negative patient outcomes [5,6].

Recently developed perfusion models describe microscale arterioles, capillaries, and venules embedded into the brain parenchyma as coupled porous media [12,14]. Similar models with multiple compartments have been developed in a more generic poroelastic framework [15,16]. These models require knowledge of anatomical (geometrical) and pathophysiological parameters, such as volumetric meshes of reconstructed brain geometries [17,18], and the permeability of microscale blood vessels [11,19,20]. The automated inference of such patient-specific parameters remains a challenge. For this reason, studies on computational perfusion simulations have been limited to less than three individuals [12–14,16]. Intervention trials typically incorporate hundreds of individuals to ensure the safety and efficacy of drugs and medical devices based on population statistics [1]. Therefore, the small sample size remains a major obstacle to the widespread application of perfusion simulations.

The present study sets out to overcome the limitation of the small sample size in perfusion simulations by integrating neuroimaging data from a healthy reference cohort. To this end, structural and perfusion-weighted MRI is utilised. The proposed method uses these clinical measurements to conduct multiple simulations that result in spatial CBF distributions directly comparable to perfusion-weighted imaging measurements in healthy reference subjects. This study investigates the suitability of a parameter inference method to capture variabilities between individuals in perfusion simulation. Emphases are placed on (i) GM and WM volumes; (ii) CBF values in GM and WM; and (iii) perfusion lesion volumes during AIS.

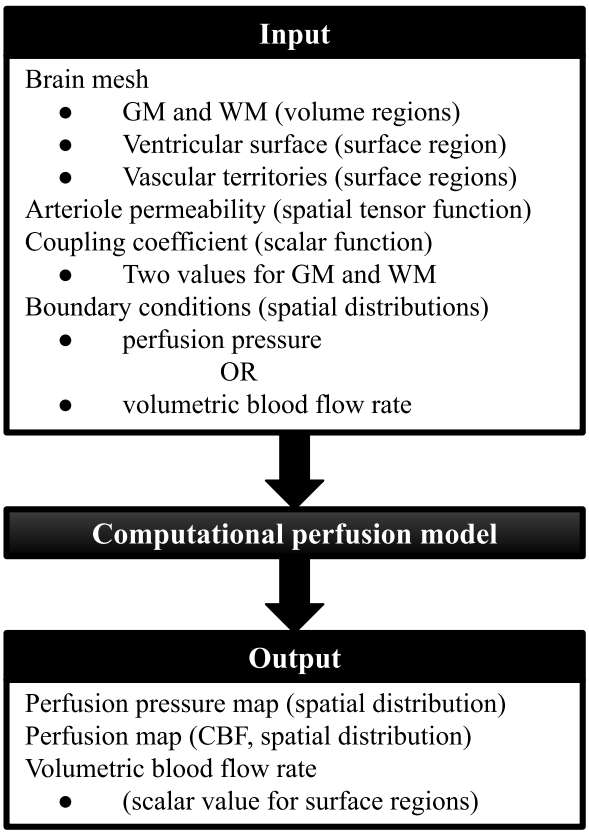


Fig. 1. Black box representation of the computational perfusion model listing input and output data. CBF — cerebral blood flow, GM — grey matter, WM — white matter.

2. Theory

This section describes the theoretical aspects of perfusion simulation. A mathematical framework is presented and linked to anatomy and physiology through parametrisation (Fig. 1). The employed perfusion model is a simplified version of previously described two- [14] and three-compartment [12,13,15,16] porous haemodynamics models. In the simpler two-compartment model, parenchymal blood vessels are categorised as arterioles, capillaries, and venules (Fig. 2). The microcirculation is then described as two porous media — accounting for arteriole and venule vessel networks. This approach relies on local "voxel-scale" space-averaged variables and macroscale parameters, such as the blood pressure and permeability tensors representing the conductance of descending arteriole and ascending venule vessel bundles. The arteriole and venule compartments are then connected by a coupling term symbolising the "voxel-scale" conductance of capillaries. Consequently, this approach does not require detailed knowledge of microscale blood vessels.

2.1. Mathematical formulation

The porous perfusion model utilised in the present study targets AIS modelling. Therefore, it focuses on the arterial side of the systemic cerebral circulation and accounts solely for a single arteriole compartment. This simplification can be derived directly from a two-compartment model [13,14] by assuming constant venule pressure (Fig. 2). Cerebral perfusion pressure (CPP) defined as the arteriole and venule pressure difference is the primary variable, with the spatial CPP distribution governed by

$$\nabla \cdot (\boldsymbol{K}\ \nabla \mathrm{CPP}) - c \cdot \mathrm{CPP} = 0. \tag{1}$$

In this section, the International System of Units (SI) is used to ease dimensional analysis so that CPP [$\mathrm{Pa} = \mathrm{kg\,m^{-1}\,s^{-2}}$]. In Eqs. (1), ∇ is the first-order spatial differential operator, Therefore, ∇CPP [$\mathrm{kg\,m^{-2}\,s^{-2}}$] is the gradient of the perfusion pressure. The first term in Eq. (1) represents fluid flow in arterioles as dictated by CPP and the permeability tensor $\boldsymbol{K}$ [$\mathrm{m^3\,s\,kg^{-1}}$] characterising descending arterioles shown in Fig. 2.

Eqs. (1) is an extended version of Darcy's law describing flow in porous media with the ratio of permeability [$\mathrm{m^2}$] and the dynamic viscosity [$\mathrm{kg\,m^{-1}\,s^{-1}}$] of the filling fluid. In the case of blood flow, viscosity depends on the pore size [21], which is not constant in the microcirculation. Therefore, these two quantities cannot be separated on a global level, and thus both of them are incorporated in the permeability tensor $\boldsymbol{K}$ [19,20].

The second term in Eq. (1) describes local drainage, which is linearly proportional to the arteriole-venule coupling coefficient, c [$\mathrm{m\,s\,kg^{-1}}$]. The $c \cdot$ CPP [$\mathrm{s^{-1}}$] term quantifies the volume of blood leaving the arteriole compartment locally in a unit time per given tissue volume. Divided by the brain tissue density ρ [$\mathrm{kg\,m^{-3}}$], it provides perfusion [$\mathrm{m^3\,s^{-1}\,kg^{-1}}$] – a term defined here interchangeably with cerebral blood flow (CBF) – as

$$\mathrm{CBF} = \frac{c \cdot CPP}{\rho}. \tag{2}$$

We assume $\rho = 1000$ [$\mathrm{kg\,m^{-3}}$] as estimates based on different measurements lie between 978 [22,23] and 1040 [$\mathrm{kg\,m^{-3}}$] [24]. The model is quasi-steady-state and does not include gravity, and thus it describes short-term-time-averaged values in a lying individual's resting state.

2.2. Parametrisation

Here, the parametrisation of the applied perfusion model is described summarising our previous work [12,13] (see Fig. 1) . To capture rapid perfusion change between grey and white matter, different coupling coefficients are allocated for the corresponding tissue regions

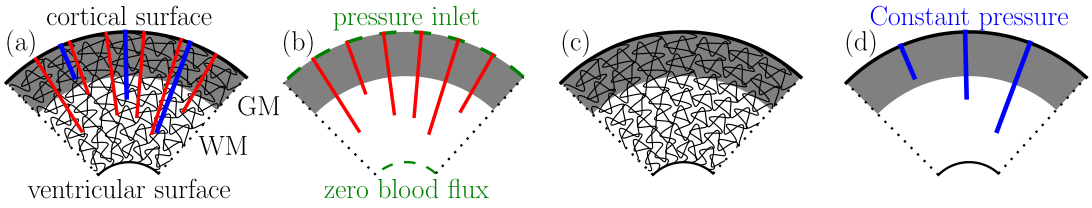


Fig. 2. Schematic of the microcirculation along a cerebral slice: descending arterioles (red), capillaries (black) and ascending veins (blue) are shown in both grey (GM) and white matter (WM) (a). The porous cerebral blood flow model relies on the idea of separating these vessels into coexisting arteriole (b), capillary (c), and venule (d) compartments. The model utilised in this study has a single arteriole compartment where boundary conditions are prescribed as indicated by the dashed green lines in (b). Capillaries (c) are taken into account with coefficients (different in GM and WM) coupling the arterioles (b) to venules represented by constant pressure (d).

Table 1
Haemodynamic parameters of the perfusion simulations considered in this study (mean ± SD). CPP — cerebral perfusion pressure, f_s — CPP scaling factor, c^{GM} and c^{WM} — grey and white matter coupling coefficients, k_{11}^{ref} — arteriole permeability in a conveniently defined reference coordinate system.

Parameter	Value	Unit	Source
CPP_h	$\approx 11330 \pm 1330$ (85 ± 10)	Pa (mmHg)	Randomised based on [26]
f_s	0.92 ± 0.01	–	Randomised based on [27]
c^{GM}	$(8.85 \pm 1.84) \times 10^{-7}$	$\mathrm{Pa^{-1}\,s^{-1}}$	From CPP_h and f_s based on Eq. (8)
c^{WM}	$(2.53 \pm 0.62) \times 10^{-7}$	$\mathrm{Pa^{-1}\,s^{-1}}$	Optimised
k_{11}^{ref}	0.18 ± 0.06	$\mathrm{mm^3\,s\,kg^{-1}}$	Optimised

denoted by c^{GM} and c^{WM}, respectively. Thereafter, a reference Cartesian coordinate system is defined to compute $\boldsymbol{K}$. The first axis of this reference coordinate system is aligned with the local centreline of descending arterioles. It is assumed herein that descending arterioles are connected solely by capillaries and therefore their permeability tensor in the reference coordinate system is

$$\boldsymbol{K}^{\mathrm{ref}} = \begin{bmatrix} k_{11}^{\mathrm{ref}} & 0 & 0 \\ 0 & 0 & 0 \\ 0 & 0 & 0 \end{bmatrix}. \tag{3}$$

From here, the anisotropic and heterogeneous $\boldsymbol{K}$ tensor field is obtained by transforming $\boldsymbol{K}^{\mathrm{ref}}$ from the local reference to the global coordinate system as detailed previously [12]. The reference coordinate system is computed from the brain geometry, assuming that: (i) penetrating arterioles descend perpendicularly to the cortical surface [25]; and (ii) arterioles follow the shortest path between the cortical and ventricular surfaces. Model parameters used in this study are summarised in Table 1.

2.3. Geometrical definition and boundary conditions

Eq. (1) is solved over the domain of interest restricted to the brain tissue denoted by Ω, comprised of grey and white matter. The bounding surfaces ($\partial\Omega$) are

1. the ventricular surfaces Γ_V; and
2. the pial surface Γ_P,

so that $\partial\Omega = \Gamma_V \cup \Gamma_P$. The boundary region associated with the pial surface is divided further into eight subregions of the major feeding arteries using a vascular territory atlas [28]. The surface regions correspond to the left and right anterior, middle and posterior cerebral arteries (six regions), the cerebellar arteries (1 region), and the perforating basilar and vertebral arteries perfusing the brain stem (1 region). This subdivision is necessary to impose boundary conditions for stroke simulations associated with major cerebral artery occlusion.

The imposed boundary conditions are:

- Blood flow rate through the ventricle surfaces (Γ_V) is zero in every case. Introducing $\boldsymbol{n}$ as the outward-pointing normal unit vector corresponding to the boundary surfaces, this Neumann type boundary condition reads as

$$\boldsymbol{K}\nabla\mathrm{CPP}\cdot\boldsymbol{n} = 0 \quad \text{on } \Gamma_V. \tag{4}$$

  Filtration through the blood-cerebrospinal fluid barrier is neglected but it could be modelled by setting a non-zero value on the right-hand side of Eq. (4) to represent fluid flux at the choroid plexus.
- The Γ_P boundary treatment distinguishes two different scenarios:
  - In healthy cases, constant cerebral perfusion pressure is prescribed (CPP_h) [13]:

$$\mathrm{CPP} = \mathrm{CPP}_h \quad \text{on } \Gamma_P. \tag{5}$$

  - To model occlusions, blood flow rate through the superficial perfusion region associated with the occluded vessel is set to zero while perfusion pressure in other regions is maintained. For example, a right middle cerebral artery (R-MCA) occlusion is captured by

$$\mathrm{CPP} = \mathrm{CPP}_h \quad \text{on } \Gamma_P \setminus \Gamma_{\text{R-MCA}}; \tag{6a}$$

$$\boldsymbol{K}\nabla\mathrm{CPP}\cdot\boldsymbol{n} = 0 \quad \text{on } \Gamma_{\text{R-MCA}}. \tag{6b}$$

Once a boundary region of the brain mesh Γ_{x} is defined, the corresponding volumetric blood flow rate Q_{x} [$\mathrm{m^3 s^{-1}}$] is computed as

$$Q_{\mathrm{x}} = \int_{\Gamma_{\mathrm{x}}} \boldsymbol{K}\nabla\mathrm{CPP}\ \mathrm{d}(\Gamma_{\mathrm{x}}\boldsymbol{n}), \tag{7}$$

where the Darcy velocity vector is $-\boldsymbol{K}\nabla\mathrm{CPP}$ so that a positive Q_{x} means that blood is delivered to the brain. Setting $\Gamma_{\mathrm{x}} = \partial\Omega$ results in the total volumetric blood flow rate to the brain (Q_t). Furthermore, $\Gamma_{\mathrm{x}} = \Gamma_{\text{L-MCA}}$ and $\Gamma_{\mathrm{x}} = \Gamma_{\text{R-MCA}}$ lead to $Q_{\text{L-MCA}}$ and $Q_{\text{R-MCA}}$, respectively. Thereafter, the representative volumetric blood flow rate of the middle cerebral arteries is obtained by averaging: $Q_{\mathrm{MCA}} = 0.5 \cdot (Q_{\text{L-MCA}} + Q_{\text{R-MCA}})$. Volumetric blood flow rates corresponding to other major cerebral arteries are obtained similarly.

3. Methods

This section covers how the parameters needed for modelling were obtained from blood pressure data from the literature [26] and neuroimaging data from a healthy reference cohort.

3.1. Participants

Reference data from $N = 84$ healthy control subjects were drawn from the v500.0 release of the European Prevention of Alzheimer's

Dementia (EPAD) study (VUmc site only) [29]. $N = 5$ subjects with missing age and/or sex information and further $N = 4$ subjects with missing structural and/or perfusion-weighted imaging data were excluded. The sample size of the resulting cohort was $N = 75$, age 68 ± 8 years, range 47–86 years, 56% female.

3.2. Image acquisition and processing

Both structural and perfusion-weighted images were obtained with a single 3T Achieva scanner (Philips Healthcare, Best, The Netherlands). Structural images were measured using T1-weighted MRI with a spatial resolution of $1.0 \times 1.0 \times 1.2$ [mm^3]. CBF was measured with a pseudo-continuous ASL (PCASL) MRI sequence with a 2D echo-planar imaging (EPI) readout and the following parameters: repetition time/echo time (TR/TE) 4800/10.4 [ms], labelling duration 1650 [ms], voxel size $3.44\times 3.44\times 4.50$ [mm^3] with 36 slices without a slice gap, and 30 control-label pairs. Post-labelling delay ranged between 2025 [ms] for the first slice and 3310 [ms] for the last slice. Two background suppression pulses were applied at 1710 and 3142 [ms] after the start of the labelling. A separate calibration M0 scan was acquired with the same acquisition protocol, but without background suppression or labelling, and with a TR of 10 [s].

Neuroimaging data were processed using the open-source ExploreASL toolbox (www.github.com/ExploreASL) with default settings [30]. In short, T1-weighted images were segmented using CAT12 [31] to obtain probability maps of grey matter, white matter, and cerebrospinal fluid, and to spatially normalise to the Montreal Neurological Institute (MNI) template of the IXI555 cohort [31,32]. The processing of ASL perfusion images included motion correction, motion outlier detection, and registration of the control-label difference perfusion-weighted maps to the segmented grey matter images using an affine registration. Partial volume correction was carried out based on the segmented GM and WM maps [33]. CBF was quantified using a single-compartment model [34]. Quality control steps included removal of subjects with large motion artefacts, failed labelling, and large macrovascular artefacts due to delayed label arrival. Quality of the ASL-T1 and T1-MNI registrations and motion correction was checked and performed again in case of a failure.

3.3. Parameter inference for computational modelling

The cerebral perfusion model is defined by a set of input parameters required to solve Eq. (1) subject to the boundary condition Eqs. (4)–(6) as summarised in Fig. 1. The proposed automated parameter inference method integrates clinical data to set up simulations accordingly, as depicted in Fig. 3.

Currently, not every model parameter can be obtained in a patient-specific manner. Some of the necessary perfusion model parameters are available directly from clinical data (e.g., brain geometry). Other parameters are (i) inferred indirectly from spatial perfusion maps [29] (arteriole permeability); (ii) obtained based on population statistics (e.g., blood pressure [26]), or (iii) inferred from pre-clinical measurements (e.g., grey matter coupling coefficient) [12]. For this reason, the perfusion model is not designed to mirror the properties of a specific individual at this stage. Instead, multiple models are introduced to be representative of the members of a patient cohort.

Parameter inference is divided into two sub-problems as shown in Fig. 3:

(1) Obtaining a tetrahedral volume mesh of the brain geometry with labelled volume and surface regions as detailed in Section 3.4;
(2) Inferring physiological parameters including the grey and white matter coupling coefficients (c^{GM} and c^{WM}) and the arteriole permeability (k_{11}^{ref}) explained in Section 3.5.

3.4. Anatomically accurate brain geometry preparation

Perfusion simulations require a volumetric brain mesh with each tetrahedron labelled either as GM or WM. Quasi-patient-specific geometries are obtained by first creating a general mesh template in standard space and then an affine registration of this template to the tissue mask of each specific subject. This approach avoids time-consuming and frail patient-specific geometry reconstruction [35]. A mesh template is prepared from the averaged T1-weighted MNI template of the IXI555 cohort [31,32], see Fig. 4(a–c).

Here, we utilise and adjust the head reconstruction algorithm implemented in SimNIBS [36] relying on the following steps: (i) segmentation using the Computational Anatomy Toolbox (CAT) [31,37]; (ii) surface reconstruction; (iii) volume mesh generation. First, the MNI template is segmented including GM, WM, and cerebrospinal fluid (CSF) masks, see Fig. 4(d–f). These masks have several limitations originating from (i) the smooth population-average image and MRI image resolution constrains, and (ii) the assumptions and simplifications in the segmentation and meshing algorithms:

A The left and right hemispheres are not well-separated;
B Connectivity between the ventricles and the subarachnoid space is inaccurate;
C Connectivity between the lateral and third ventricles, and the surrounding tissue is inaccurate;
D Connectivity between the third and fourth ventricles is inaccurate;
E Connectivity of tissue and CSF spaces is inaccurate (i.e. there is no direct connection between WM and CSF regions).

Limitations A-D are addressed after segmentation by employing standard image processing algorithms and manual amendments. The mask of the ventricles is altered manually based on the original segmentation and the T1-weighted template to incorporate the lateral, third and fourth ventricles in a single coherent region. Furthermore, the overall tissue mask is eroded to ensure that anatomical domains are well-separated. Ventricles are separated deliberately from the subarachnoid space to ease the imposition of boundary conditions. Fig. 4(g–i) depict the resulting adjusted segmentation.

The default SimNIBS segmentation and the corresponding mesh (referred to as Mesh A) are shown in Figs. 4(d–i) and 5(a–b), respectively. The mesh generation algorithm in SimNIBS relies strongly on a non-anatomical tissue layering assumption. Accordingly, the CSF layer is followed strictly by a GM and then a WM layer as indicated by the E1 and E2 annotations in Fig. 4(d–i). This final issue has to be corrected by post-processing the mesh corresponding to the adjusted segmentation shown in Fig. 4(g–i). Consequently, tetrahedral GM elements are relabelled in the vicinity of the ventricles and the brain stem based on the original CAT [31,37] segmentation registered to the mesh. Furthermore, tetrahedral WM elements are relabelled in the vicinity of the cortical surface to ensure that the corresponding GM thickness is at least ≈ 2 [mm] [38]. (A similar relabelling routine has been implemented previously in the Brain2Mesh toolbox [18] to address similar issues.) The resulting mesh is shown in Fig. 5(d–f) and is referred to as Mesh B. The overall fitness of Mesh A (SimNIBS default) and Mesh B was evaluated based on GM and WM anatomy and volume ratios compared to the T1-weighted MRI measurements of the EPAD cohort.

The next step is to generate a voxelised mesh template. Voxelisation is carried out using a ray intersection method [39]. Thereafter, the patient-specific T1-weighted MRI scan is segmented with CAT12 [31,37] to obtain a binary tissue mask by thresholding GM and WM probability maps at 0.5. It is worth acknowledging that a higher threshold would result in a smaller total brain volume [40]. A threshold of 0.5 was selected *a priori* because the patient-specific tissue mask is used to register the voxelised mesh mask which does not account for

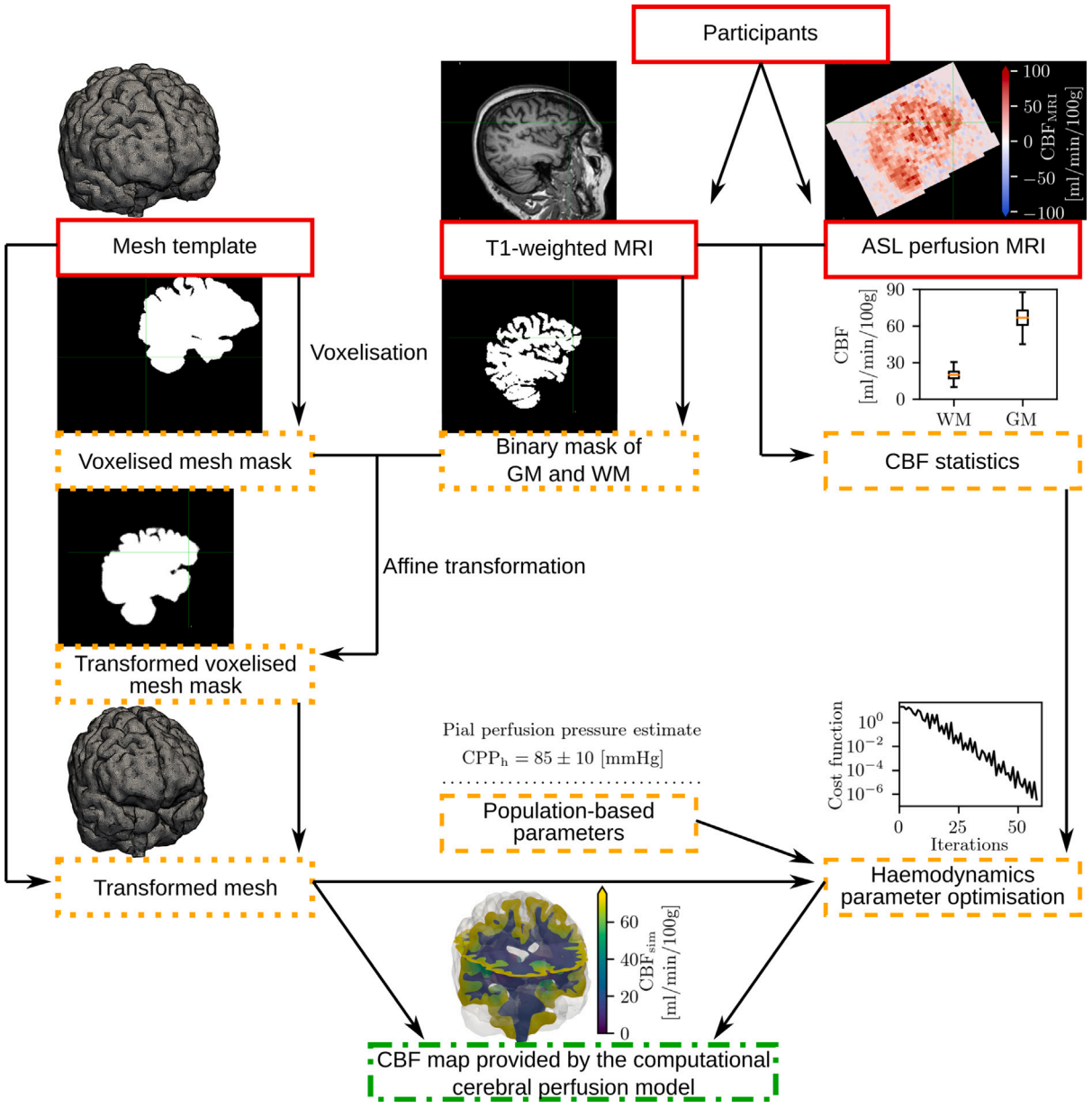


Fig. 3. Schematic drawing showing how clinical data is used to provide input for the computational perfusion model. Solid boxes: primary derivatives of clinical data; dash-dotted box: computational perfusion model; dotted boxes: quasi-patient-specific brain mesh generation; dashed boxes: haemodynamic parameter tuning. ASL — arterial spin labelling, MRI — magnetic resonance imaging, CBF — cerebral blood flow, GM — grey matter, WM — white matter, CPP — cerebral perfusion pressure.

partial volume effects. This choice is verified by the resulting brain volume assessment as detailed in Section 4.1. The voxelised mesh mask is registered to the patient-specific tissue mask using an affine transformation with 12 degrees of freedom as implemented in the FSL Linear Image Registration Tool (FLIRT) [41], part of the Oxford Centre for Functional MRI of the Brain (FMRIB) Software Library (FSL) [42]. The transformation is applied to the mesh template resulting in a quasi-patient-specific transformed mesh.

3.5. Physiological parameter optimisation

Psychological parameters of the perfusion model are obtained from clinical data and literature either as individual values or as population statistics. Perfusion statistics are extracted from patient-specific T1-weighted and ASL MRI scans (Fig. 3) based on the following quantities: (i) mean CBF in GM (CBF^{GM}_{MRI}); (ii) mean CBF in WM (CBF^{WM}_{MRI}); (iii) 20th percentile of CBF (CBF^{min}_{MRI}); 80th percentile of CBF (CBF^{max}_{MRI}). The "MRI" subscript distinguishes quantities deduced from structural/perfusion-weighted images from results originating from simulations ("sim" subscript).

Physiological parameter initialisation and optimisation based on the aforementioned perfusion statistics follow a similar strategy as in [12]. Population-based parameters are incorporated from the literature as detailed below.

1. Based on rodent experiments [27], pial perfusion pressure (CPP_h) is well-approximated by the diastolic blood pressure. Therefore, CPP_h is sampled randomly for each computational model based on diastolic blood pressure measurements in ischaemic stroke patients (Gaussian distribution assumed with mean and standard deviation as reported in [26]). The applied CPP estimation is justified based on an alternative calculation presented in Appendix.

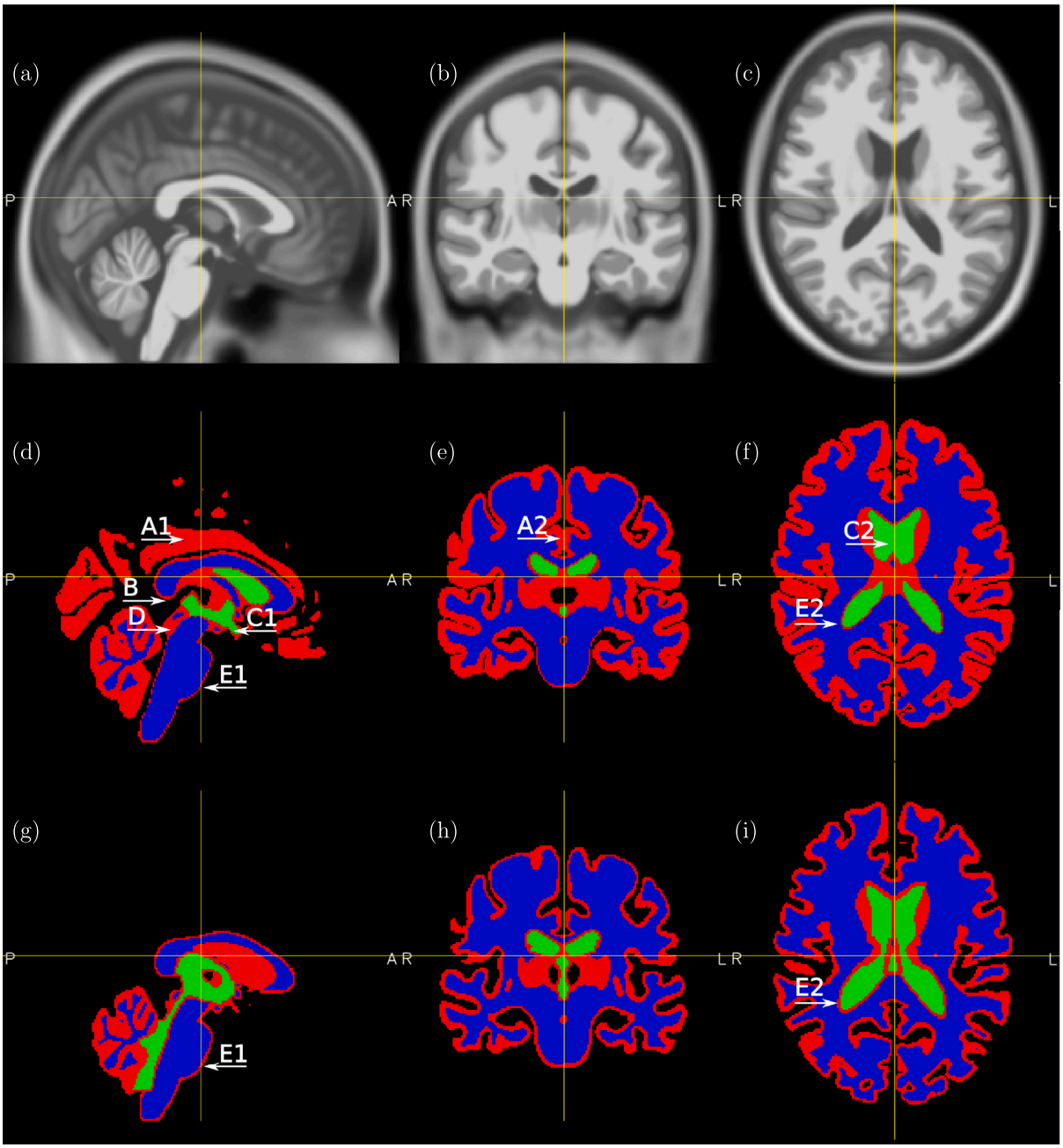


Fig. 4. Visualisation of the T1-weighted MRI MNI atlas of the IXI555 cohort [31,32] (a–c). Default SimNIBS [36] segmented images (d–f) and altered grey and white matter masks (g–i). Sagittal (a,d,g), coronal (b,e,h), and axial (c,f,i) slices. Colouring of (d–i): red — grey matter; blue — white matter; green — ventricles. The arrows indicate anatomical flaws in the segmentation: A — connected hemispheres; B — inaccurate opening between the subarachnoid space and the third ventricle; C — incomplete segmentation of ventricles; D — aqueduct of Sylvius labelled as grey matter; E — simplified tissue layering assumption.

2. For a given $\mathrm{CBF}_{\mathrm{MRI}}^{\mathrm{GM}}$ and CPP_h pair, the GM coupling coefficient is estimated as

$$c^{\mathrm{GM}} = \frac{\mathrm{CBF}_{\mathrm{MRI}}^{\mathrm{GM}} \cdot \rho}{f_s \cdot \mathrm{CPP}_h}. \tag{8}$$

Here, f_s is a scaling factor to represent the average arteriole perfusion pressure in the GM as a fraction of the boundary pressure (CPP_h).

3. Parameters k_{11}^{ref} and c^{WM}, are obtained by minimising the cost function. A penalty term (J_{penalty}) is applied to constrict CBF between the predefined minimum and maximum:

$$J = (\mathrm{CBF}_{\mathrm{MRI}}^{\mathrm{GM}} - \mathrm{CBF}_{\mathrm{sim}}^{\mathrm{GM}})^2 + (\mathrm{CBF}_{\mathrm{MRI}}^{\mathrm{WM}} - \mathrm{CBF}_{\mathrm{sim}}^{\mathrm{WM}})^2 + J_{\mathrm{penalty}} \tag{9}$$

$$\begin{aligned} J_{\mathrm{penalty}} = {} & H(\mathrm{CBF}_{\mathrm{MRI}}^{\mathrm{min}} - \mathrm{CBF}_{\mathrm{sim}}^{\mathrm{min}}) \cdot (\mathrm{CBF}_{\mathrm{MRI}}^{\mathrm{min}} - \mathrm{CBF}_{\mathrm{sim}}^{\mathrm{min}})^2 + \\ & H(\mathrm{CBF}_{\mathrm{sim}}^{\mathrm{max}} - \mathrm{CBF}_{\mathrm{MRI}}^{\mathrm{max}}) \cdot (\mathrm{CBF}_{\mathrm{MRI}}^{\mathrm{max}} - \mathrm{CBF}_{\mathrm{sim}}^{\mathrm{max}})^2. \end{aligned} \tag{10}$$

Here, H is the Heaviside function resulting in a non-zero J_{penalty} only if the $\mathrm{CBF}_{\mathrm{sim}}^{\mathrm{min}}$ and $\mathrm{CBF}_{\mathrm{sim}}^{\mathrm{max}}$ extrema are out of the target range determined by ASL MRI data.

3.6. Acute ischaemic stroke simulations

Total occlusion of the middle cerebral artery is simulated using the 75 inferred brain geometries by setting blood flow rate through the

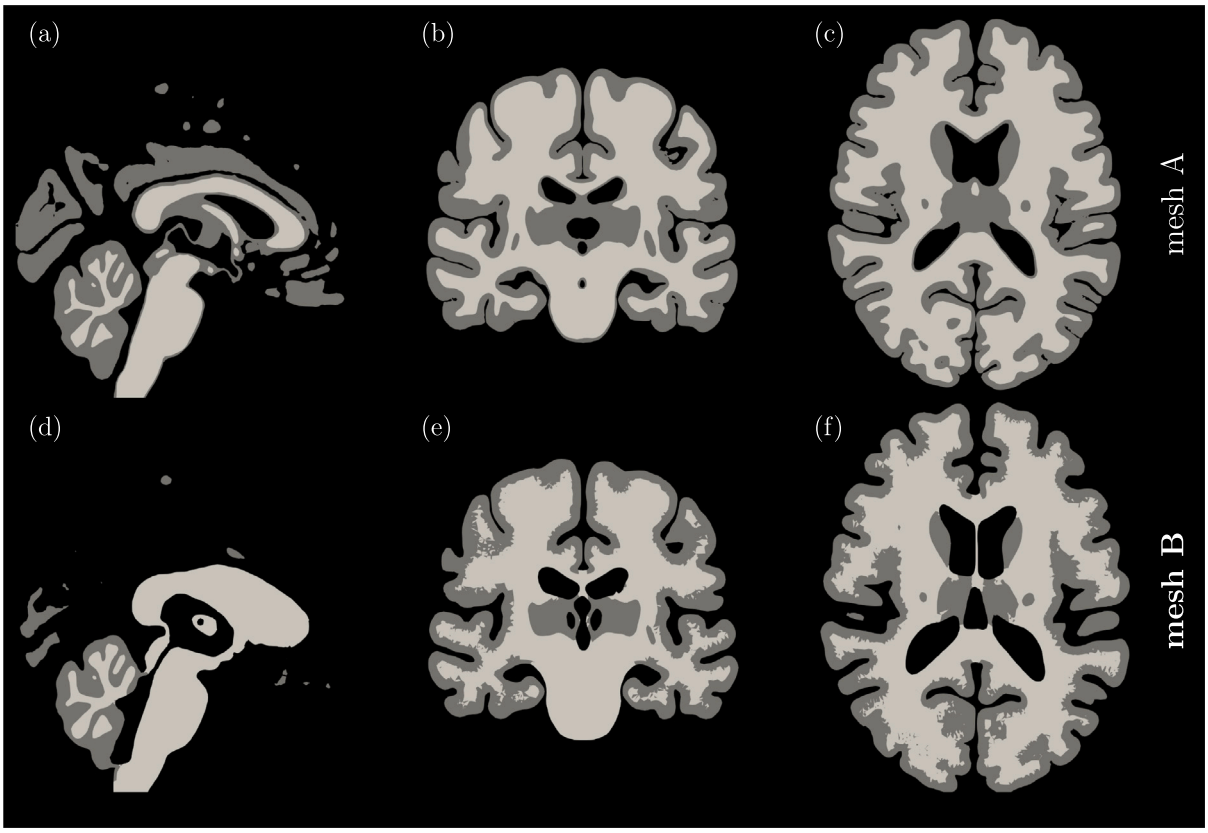


Fig. 5. Visualisation of the grey and white matter domains of two meshes along sagittal (a,d), coronal (b,f), and axial (c,f) slices. SimNIBS [36] default Mesh A (a–c) generated from the segmentation shown in Fig. 4(d–f). Mesh B (d–f) generated from the adjusted segmentation shown in Fig. 4(g–i). After a careful evaluation of the meshes, Mesh B is chosen as the mesh template in Fig. 3.

boundary region corresponding to the single occluded vessel to zero, see Eq. (6). Regarding every other model parameter, AIS simulations are identical with the healthy baseline cases. Middle cerebral artery occlusions were chosen because they are responsible for more than 60% of AIS cases [43]. Both left and right hemisphere occlusions are simulated resulting in 150 different AIS cases. Two methods are used to delineate the infarct volume based on the simulated CBF images:

1. IV_r – the region with a relative perfusion drop of 70% compared to the baseline (healthy) case, see Fig. 10(b) [44].
2. IV_a – the region with an absolute perfusion value below 5 [ml/min/100g].

It has been demonstrated previously that simulating a complete MCA blockage might lead to $\mathrm{IV}_r = 0$ unless haemodynamic parameters of the perfusion model are tuned carefully [12]. Therefore, we found comparing the distribution of the IV_r and IV_a infarct proxies to clinical data with boxplots suitable for validation. To this end, infarct quantifications from T2-weighted MRI measurements are considered corresponding to AIS patients with MCA occlusions and with 3 months outcomes of "dependent" or "dead" [45]. Beyond infarct size quantification, the location and extent of the simulated perfusion lesions are also inspected visually by comparing the estimated infarct region to a noncontrast computed tomography measurement [46] of a typical stroke patient with low collateral and recanalisation scores (patient description and image are available in [12]).

3.7. Numerical solution

Numerical solutions of the governing equations are obtained using the finite element method as implemented in the open-source FEniCS library [47]. The brain geometry is captured by tetrahedral elements. The weak form of Eq. (1) is discretised using second-order Lagrange elements for p, and zeroth-order discontinuous Galerkin elements for the permeability tensor $\boldsymbol{K}$ and the coupling coefficient c. For further details of the numerical solution of the governing equations, we refer to [12,13].

3.8. Statistical analysis

The anatomical and physiological fitness of the 75 computational models are investigated by means of linear regression analyses between variables measured in healthy reference subjects with MRI and brain models. The variables of interest selected for regression analyses are not used directly for the parameter tuning of the models. These variables include grey and white matter volumes (GMV and WMV), and the total volumetric blood flow rate to the brain (Q_t). Pearson correlation coefficients (Pearson's r) are computed between simulated and MRI samples utilising the "linregress" function of the SciPy [48] open-source Python library which relies on the P-value of the Wald test to evaluate statistical significance. The corresponding null hypothesis is that the slope of the linear regression model is zero which is rejected if the usual condition of $P < 0.05$ is met. Pearson's $r = 1$ represent the peak anatomical and physiological fitness of the computational models indicating "perfect matches" between the results of the tuned simulations and the structural and perfusion-weighted MRI measurements of the EPAD cohort.

Additionally, Mesh A and mesh B are evaluated by calculating the deviation of average volume ratios from the EPAD dataset which enables comparison with publicly available meshes obtained, for example, from the New York Head Model (NYHM) [17]. To this end, GMV and WMV normalised by the intracranial volume (ICV) are computed. Thereafter, the obtained mean values are compared to volume ratio

Table 2
Comparison of simulations and clinical measurements corresponding to healthy reference subjects and to reference data from the literature. Mean ± standard deviation values are shown as applicable. Anatomical variables include TBV — total brain volume (sum of GM and WM); GMV — grey matter volume; WMV — white matter volume; ICV — intracranial volume; A_{total} - total brain surface area; $A_{cortical}$ - cortical surface area. Physiological variables include volumetric blood flow rates corresponding to the entire brain (Q_t), and the anterior Q_{ACA}, middle Q_{MCA}, and posterior Q_{PCA} cerebral arteries. Reference data are gathered from the following sources: (i) Nielsen et al. [36]*: default SimNIBS head model (mesh A); (ii) Huang et al. [17]†: NYHM — New York Head Model, age range 18.5–43.5; (iii) Ikram et al. [49]‡: T1-weighted and T2-weighted MRI, 490 subjects, 249 women, 73 ± 8 years old; (iv) Lüders et al. [23]§: T1-weighted MRI, 100 subjects, 50 women, 25 ± 4 years old; (v) Winkler et al. [50]¶: T1-weighted MRI-based surface reconstruction; (vi) Zarrinkoob et al. [51]‖: phase-contrast (PC) MRI, 45 subjects, 23 women, 71 ± 4 years old. (vii) Xing et al. [52]**: PC MRI, 39 subjects, 24 women, 71 ± 4 years old.

	Brain models	EPAD [29]	Reference data	
			Value	Source
TBV/ICV [%]	71.4	74.1 ± 4.0	78.8	mesh A [36]*
			83.3	NYHM [17]†
			77.4 ± 3.7	MRI [49]‡
GMV/ICV [%]	38.1	39.9 ± 2.6	41.9	mesh A [36]*
			49.2	NYHM [17]†
			55.1 ± 2.0	MRI [23]§
			46.6 ± 4.0	MRI [49]‡
WMV/ICV [%]	33.3	34.2 ± 2.2	36.9	mesh A [36]*
			34.1	NYHM [17]†
			27.4 ± 2.0	MRI [23]§
			30.8 ± 5.7	MRI [49]‡
A_{total} [cm^2]	2040	—	2262	mesh A [36]*
			1774	NYHM [17]†
$A_{cortical}$ [cm^2]	1659	–	1770	MRI [50]¶
Q_t [ml/min]	424 ± 73	463 ± 84	657 ± 94	PC MRI [51]‖
			488 ± 123	PC MRI [52]**
Q_{ACA} [ml/min]	48 ± 8	–	75 ± 15	PC MRI [51]‖
Q_{ACA}/Q_t [%]	11 ± 2	–	11 ± 2	
Q_{MCA} [ml/min]	85 ± 15	–	131 ± 23	
Q_{MCA}/Q_t [%]	20 ± 4	–	20 ± 4	
Q_{PCA} [ml/min]	47 ± 8	–	51 ± 10	
Q_{PCA}/Q_t [%]	11 ± 2	–	8 ± 2	

measurements from the segmented T1-weighted images of the EPAD cohort. In this context, the superior anatomical fitness of a mesh manifests in smaller GMW/ICV and WMV/ICV differences compared to reference values.

4. Results

In the following sections, units are presented based on clinical conventions (e.g., volume in ml, CBF in ml/min/100g) to facilitate comparisons with other studies.

4.1. Validation of modelled brain volumes

Fig. 5 highlights several qualitative geometrical differences between Mesh A and Mesh B. A smooth grey-white matter interface cannot be preserved in Mesh B because of the relabelling required for preserving anatomical structures. Nevertheless, the GM regions of Mesh B remain continuous with three well-separated territories corresponding to the two hemispheres and the cerebellum. Such qualitative anatomical details are not preserved by Mesh A.

The first half of Table 2 aims to evaluate the utilised mesh template (Mesh B) compared to other head models including Mesh A (SimNIBS default) [36] and the NYHM. The total brain volume (TBV), GMV and WMV normalised by the ICV are representative of the EPAD healthy senior population both in Mesh A and Mesh B. The GMV/ICV ratio distribution of the EPAD population indicates low brain atrophy [53] irrespective of the large age span of the cohort. The root-mean-square error of the GMV/ICV and WMV/ICV ratios of Mesh A and the NYHM compared to the EPAD mean value measurements is 2.4% and 6.6%, respectively. By comparison, the total error of Mesh B is 1.4% indicating better anatomical fitness compared to Mesh A and the NYHM. Therefore, Mesh B was selected as the default mesh template for simulations of senior adults. The brain tissue volume statistics of the resulting computational models are in good agreement with the T1-weighted MRI measurements of the EPAD cohort, as summarised in Table 3.

Table 3
Statistical analysis of the brain anatomy (geometry) and physiology (haemodynamics) of healthy control subjects and computational models (transformed Mesh B): SD — standard deviation; GMV — grey matter volume; WMV — white matter volume; Q_t — total volumetric blood flow rate to the brain.

	Computational models mean ± SD	EPAD [29] mean ± SD	Pearson's r	P-value
GMV [ml]	620 ± 63	593 ± 49	0.74	<0.001
WMV [ml]	542 ± 55	510 ± 61	0.84	<0.001
Q_t [ml/min]	424 ± 73	463 ± 84	0.89	<0.001

Fig. 6(a) highlights discrepancies between the tissue masks of models (transformed Mesh B) and healthy control subjects (EPAD), which are typically located near the boundary of the tissue geometry. The total brain volume of healthy controls tends to be overestimated by 58 ml (on average 5%) by the corresponding brain models, see Fig. 6(b).

4.2. Haemodynamic analysis of the computational models

The cost function trends corresponding to the physiological parameter optimisation are displayed in Fig. 7(a) and the resulting parameters are listed in Table 1. In ≈ 57% of the cases, the square root of the cost function ($\sqrt{J}$) drops below one, meaning that the target grey and white matter CBF values are met within the specified minimum and maximum limits with a deviation less than 1 [ml/min/100g]. The optimisation leads to a final $\sqrt{J} < 10^{-2}$ in 20 out of 75 cases. CBF values displayed in Fig. 7(b–c) indicate that the simulations overshoot regional target values in every case. In the worst-case distinguished in Fig. 7(a–c), $\sqrt{J} \approx 3$ [ml/min/100g] is reached. This relatively large difference is caused by a mismatch between the targeted and the reached average grey matter perfusion values as suggested by Fig. 7(b).

The second half of Table 2 presents a comparison of blood flow rate information obtained from simulations and clinical neuroimaging datasets. The Q_t distribution resulting from simulations (and the EPAD ASL perfusion MRI measurement) agree well with previous clinical PC MRI measurements [52]. Conversely, the simulated blood flow rates in major cerebral arteries are significantly lower than reported previously [51]. However, normalised blood flow rates in major cerebral arteries (e.g., Q_{MCA}/Q_t) are in satisfactory agreement with previous measurements [51].

Considering the total volumetric blood flow rate to the brain (Q_t), simulations are in agreement with values inferred from ASL perfusion MRI of healthy reference individuals in EPAD as detailed in Table 3. Volumetric blood flow rates in computational brain models tend to be underestimated on average by 8%. The average CBF in perfusion models is 37 [ml/min/100g] whereas the average CBF of healthy references in the EPAD cohort is 42 [ml/min/100g] based on the corresponding ASL MRI measurements. Whereas average grey and white matter perfusions are matched by the optimisation algorithm, computational models underestimate total brain perfusion on average by 12%. This relatively high error originates from the overestimation of the brain volume and the underestimation of the total volumetric blood flow rate. This finding suggests that meshes with good anatomical fitness are necessary but not sufficient to obtain models with good physiological fitness. Nevertheless, Pearson's r and the P-value presented in Table 3 emphasise a strong, statistically significant correlation between the

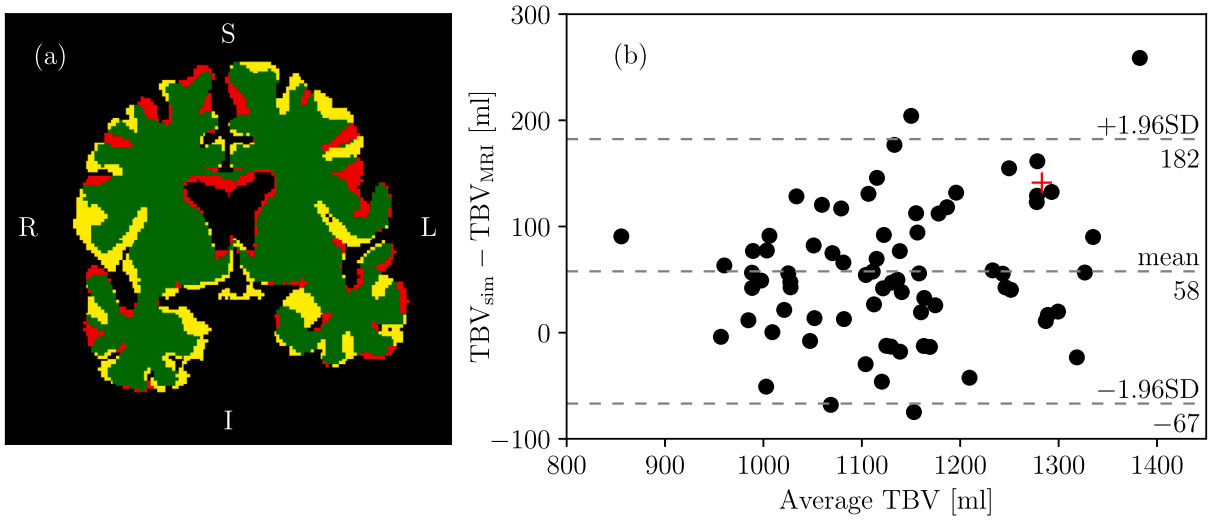


Fig. 6. Comparison of the tissue mask corresponding to a healthy reference subject (sum of grey and white matter probability maps larger than 0.5) and the associated transformed voxelised mesh mask (a): green — overlap; yellow — reference only; red — perfusion model only. Bland-Altman plot comparing total brain volumes (TBV - sum of GM and WM) corresponding to reference subjects (TBV_{MRI}, measured as the sum of grey and white matter probability maps) and the associated quasi-patient-specific transformed mesh (TBV_{mesh}) (b). The red + symbol in (b) marks the patient shown in (a). L — left, R — right, S — superior, I — inferior, SD — standard deviation.

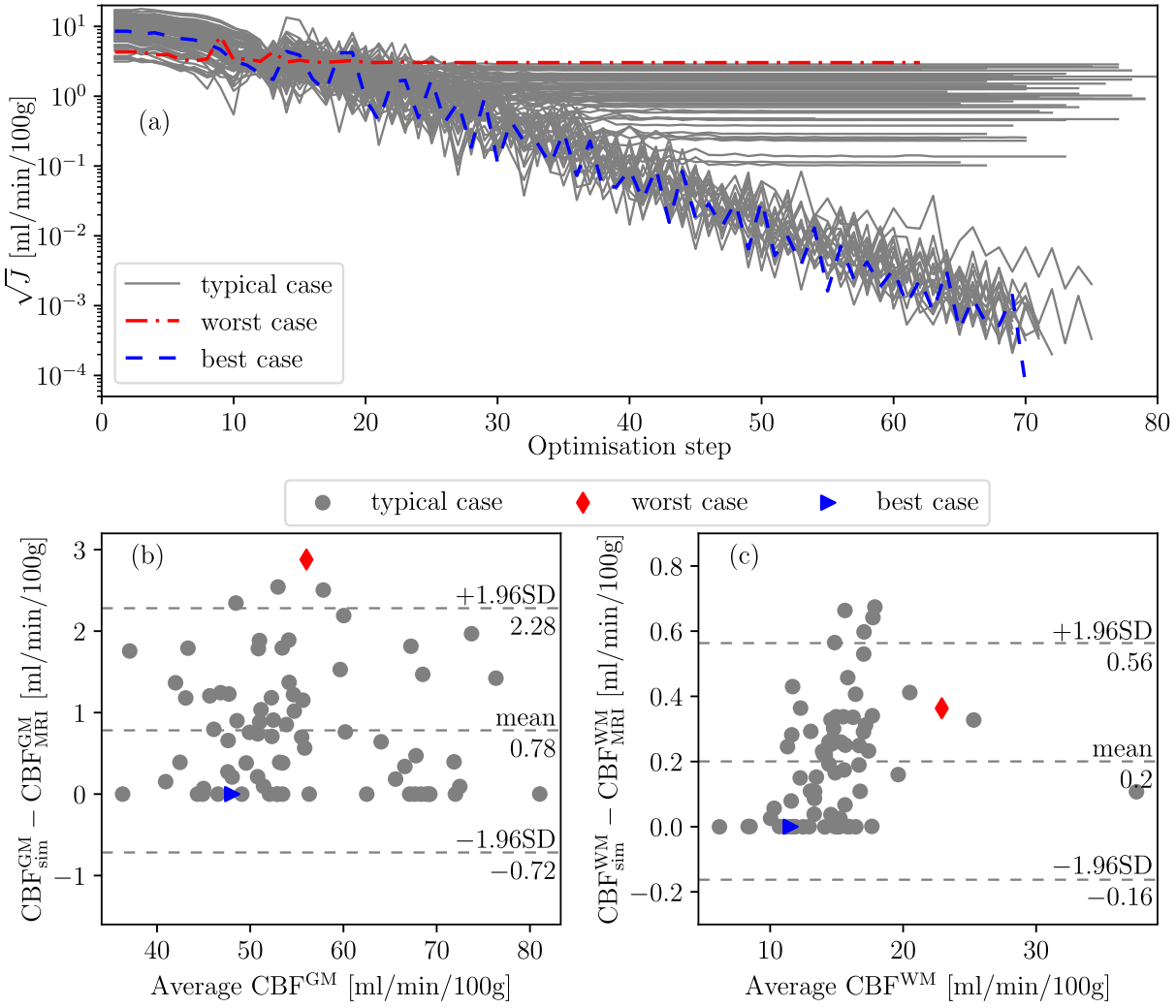


Fig. 7. Cost function (J) convergence trends as functions of the optimisation steps (a); Bland-Altman plots of the mean white matter perfusion CBF^{WM} (b) and mean grey matter perfusion CBF^{GM} (c) of computational brains and healthy references. Worst and best cases correspond to the highest and lowest final cost function values, respectively. The subscripts "sim" and "MRI" distinguish data corresponding to simulations and ASL perfusion MRI, respectively. CBF — cerebral blood flow, SD — standard deviation.

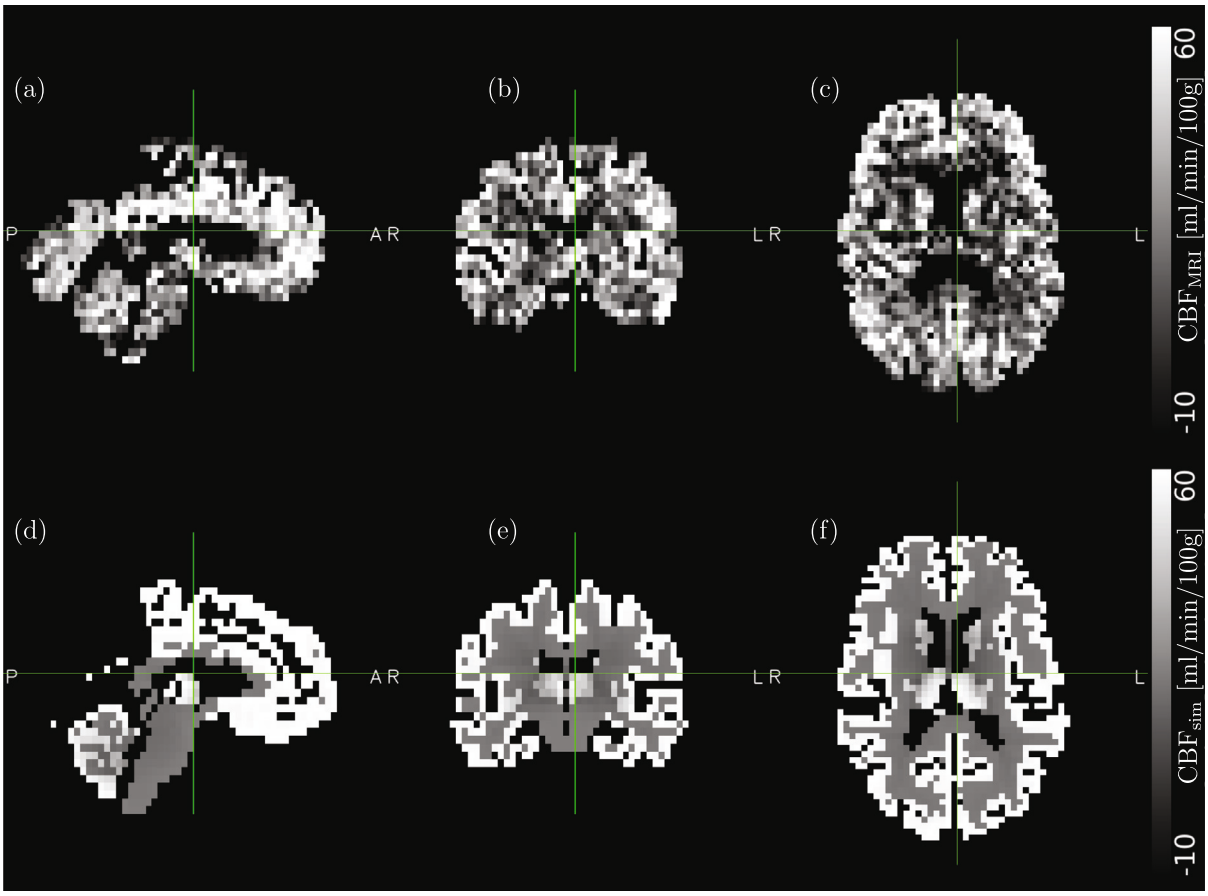


Fig. 8. Cerebral blood flow (CBF) maps of a healthy reference individual from the EPAD project (a–c) and the corresponding simulation (d–f) along sagittal (a,d), coronal (b,f), and axial (c,f) slices. In the case if (a–c), MRI results are multiplied by a binary tissue mask which corresponds to regions where the sum of the grey and white matter probability maps is higher than 0.5. The subscripts "sim" and "MRI" distinguish data corresponding to simulations and ASL perfusion MRI, respectively. Simulation data linked to the worst-case highlighted in Fig. 7.

total blood flow rates measured in healthy reference subjects and in the computational models.

Fig. 8(a–c) and (d–f) visualise 3D CBF maps corresponding to a clinical measurement and the linked brain model. Perfusion distribution in the computational model appears to be relatively homogeneous compared to clinical measurements. The perfusion model parameters could thus be tuned further to achieve better agreement with clinical data representing instantaneous averaged perfusion state. Instead, we recommend interpreting simulation results as short-term time-averaged measurements which are reminiscent of clinical studies reporting ensemble-averaged perfusion maps [54].

The probability density functions displayed in Fig. 9 confirm that the simulated grey and white matter regions have well-distinguishable perfusion values. This is also visible in Fig. 8(d–f). By comparison, the probability density function of ASL perfusion MRI shows a nearly Gaussian trend with standard deviation in the same order of magnitude as its mean value. This is probably caused by (i) the relatively low signal-to-noise ratio of ASL perfusion MRI, and (ii) the continuous fluctuations of local cerebral perfusion associated, e.g., with neurovascular coupling.

4.3. Infarct volume estimation in acute ischaemic stroke

Perfusion pressure and perfusion distributions in a typical occluded scenario are visualised in Fig. 10(a) and (b), respectively. Both infarct proxies result in similar, approximately normally distributed, infarct volume estimates as shown in Fig. 11. Mean and standard deviation values in the case of the relative perfusion drop based infarct volume proxy (IV_r) are 205 ± 23 ml. By comparison, IV_a leads to somewhat smaller infarct estimations with higher variance: 197 ± 25 ml.

5. Discussion

This study has three main findings. Firstly, the proposed approach of rapid, group-level mesh generation which relies on the geometrical transformation of a mesh template, captures primary anatomical differences in healthy, senior populations. These differences cover variance in tissue volumes and simple shape differences but exclude variance in tissue volume ratios. Secondly, haemodynamic parameters are inferred successfully from ASL MRI data as suggested by the overlap between CBF values obtained from clinical measurements and simulations. Finally, the computational perfusion model appears to predict the impact of large artery occlusion on spatial CBF distribution reliably at the population level. Even though, it is important to notice, that the physiological variability of CBF in a healthy population cannot explain the high variability of the infarct volume in AIS patient cohorts.

Cohort-level simulations have been identified as a requirement for *in silico* ischaemic stroke trials [5]. Difficulties associated with the parameter inference of perfusion models limited the sample size of simulations as reported in several previous studies [12,55,56]. The proposed approach enables perfusion simulations in a relatively large cohort by automating parameter inference from neuroimaging data. This study builds on a recently established method for haemodynamic parameter inference [12]. Furthermore, brain geometries are obtained here by geometrical transformations instead of patient-specific image processing and meshing, which appeared as a major bottleneck of automation in previous studies [12,14,16,55,56].

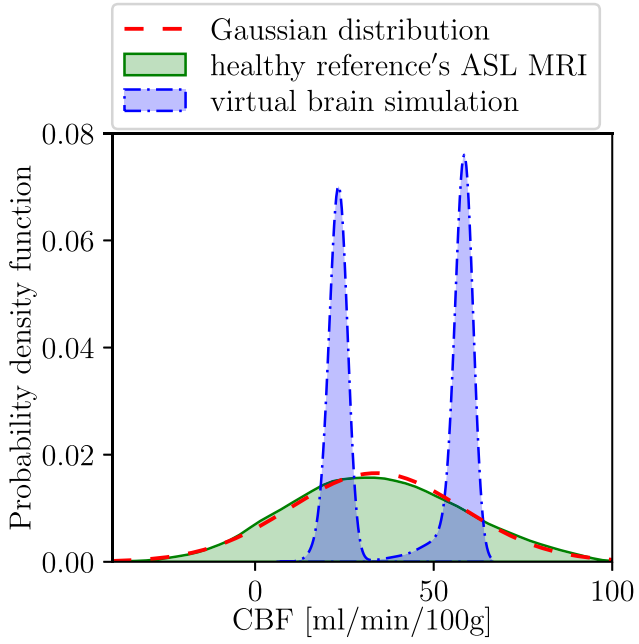


Fig. 9. Probability density functions of cerebral blood flow (CBF) maps. The subscripts "sim" and "MRI" distinguish data corresponding to simulations and arterial spin labelling (ASL) perfusion MRI, respectively. MRI results are multiplied by a binary tissue mask labelling regions where the sum of the grey and white matter probability maps is higher than 0.5. The perfusion maps of a healthy reference subject providing the input for this graph are displayed in Fig. 8. The distribution of CBF_{MRI} data is well approximated by the Gaussian function (mean±SD: 34 ± 24 [ml/min/100g]). SD — standard deviation.

5.1. Anatomical evaluation

Obtaining computational geometries for physiological simulations is a non-trivial task. In the present study, we propose the creation of a mesh template as an intermediate step towards the standardisation of computational geometries. Thereafter, quasi-patient-specific geometries can be obtained by rapid and robust transformations (i.e. affine) instead of relying on resource-intensive, and fragile mesh generation algorithms. The mesh template plays a critical role in the present cohort-level modelling approach because any issues of the mesh template are naturally "inherited" by the generated brain models.

The TBV/ICV, GMV/ICV and WMV/ICV tissue volume ratios of the computational brains and the EPAD cohorts are lower than the reported values in previous neuroimaging studies [23,49]. The differences are obvious especially when data from the present study are compared with values reported in the MRI study of Lüders et al. [23] and with measurements of the NYHM [17]. It is important to acknowledge that these datasets correspond to healthy young reference subjects (details in the caption of Table 2). Therefore larger TBV/ICV, GMV/ICV, and WMV/ICV tissue volume ratios are not surprising compared to the present investigation which focuses on healthy senior references. This comparison highlights that it might be necessary to utilise different mesh templates for the simulations of cohorts with different age groups.

To date, only a few studies considered physiological simulations of human brains at the level of patient cohorts [57]. State-of-the-art segmentation [31,58–60] and mesh generation techniques [18,36,57] are often computationally more expensive than all the other steps shown in Fig. 3 and they have not been designed to satisfy requirements for perfusion simulations. The proposed perfusion model generation method sacrifices patient-specific mesh generation to enable cohort-level organ-scale cerebral perfusion simulations.

Publicly available head or brain meshes reflect well the challenges associated with automated, anatomically accurate patient-specific mesh generation. For example, Mesh A [36], the NYHM [17] and the finite element mesh of Garcia-Gonzalez et al. [61] suffer from qualitative and

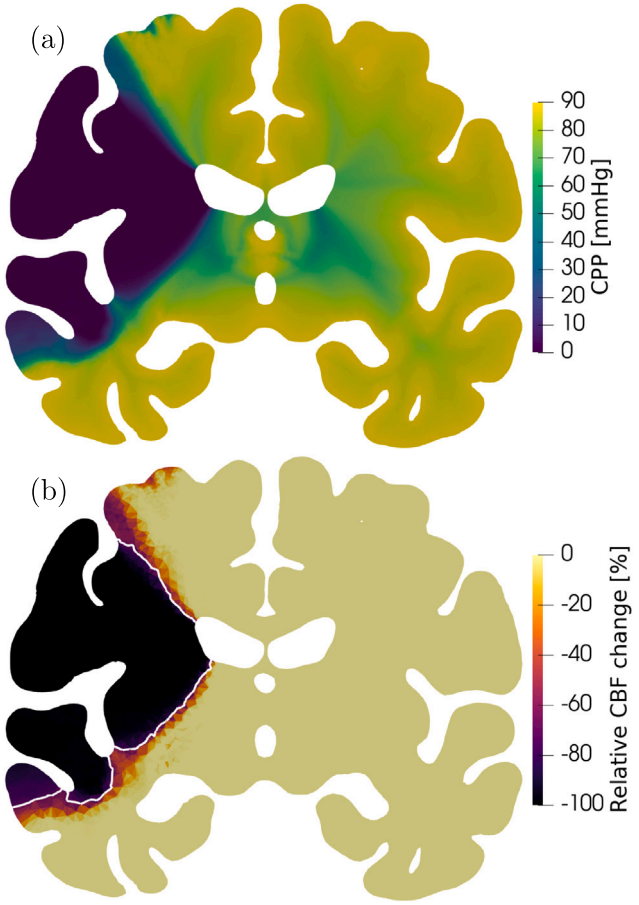


Fig. 10. Simulation results in an occluded case. Perfusion model parameters are inferred from MRI data of the individual shown in 8(a–c): CPP — cerebral perfusion pressure (a) and relative cerebral blood flow (CBF) change in addition to isolines indicating 70% CBF drop used to define IV_r, the infarct volume based on relative CBF change (b).

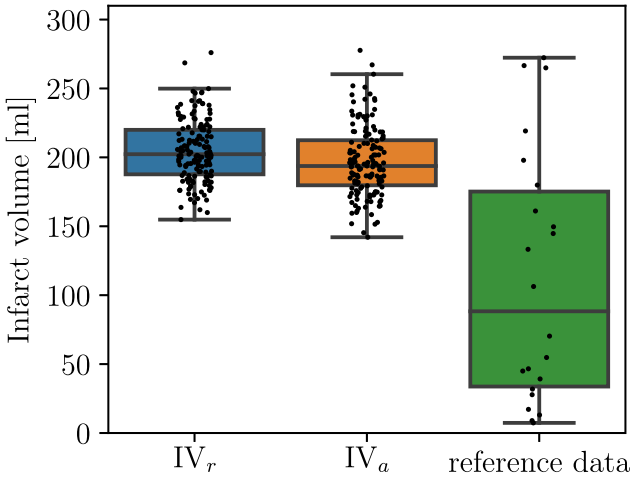


Fig. 11. Comparison of infarct volume proxies defined based on relative cerebral blood flow (CBF) change (IV_r) and from the absolute CBF level (IV_a). Required CBF maps determined by middle cerebral artery occlusion simulations. The reference data [45] correspond to T2-weighted magnetic resonance imaging of acute ischaemic stroke patients with middle cerebral artery occlusions.

quantitative anatomical flaws of the grey and white matter distributions (see also Figs. 4(d–f) and 5(a–c) and Table 3). The aforementioned head models were designed for eletrophysiological and tissue deformation simulations where usually the entire head is modelled and thus misrepresentations of the brain parenchyma might be less important. However, in haemodynamics simulations, these artefacts (e.g. an incorrect tissue region between the hemispheres) manifest into non-physiological blood flow pathways.

5.2. Physiological evaluation in health and disease

The proposed computational model produces results visually similar to averaged perfusion maps measured in clinical scenarios [54,62]. Consequently, group-level simulations with parameters inferred from MRI capture the between-subject variability of CBF both in GM and WM. The inferred haemodynamic parameters have low variance compared to the corresponding mean values irrespective of the relatively large age range of the EPAD cohort, the variance of the assumed blood pressure and the perfusion measured by ASL MRI. However, the uncertainties of the computational perfusion model are tied to the uncertainties of the employed MRI techniques. Therefore, the coupling coefficient of the WM (c^{WM}) is burdened by a relatively high uncertainty because of the relatively low signal-to-noise ratio of ASL MRI in WM [34]. In the population providing the reference data, the lowest average CBF values in WM lie between 5 and 10 [ml/min/100g] as shown in Fig. 8(c). These values are inherited by the simulations as dictated by the parameter optimisation and ASL MRI which might produce unreliable CBF estimates in WM.

The present simulation results are expected to represent worst-case scenarios with relatively large infarct volume estimates because of the complete blockage of the middle cerebral artery. Clinical patients' lesions have higher between-subject variance and the worst-case scenarios simulated in this study can explain only half of the clinically measured infarct volume distribution [45]. In particular, the presented simulations capture solely the largest infarcts ranging from about 140 to 275 [ml] whereas the range of clinical measurements is approximately between 5 and 275 [ml]. Such predictions occur probably because the present simulations do not account for compensatory mechanisms – such as blood flow rerouting through collaterals [2,63] and autoregulation [64] – which could help to restore perfusion levels after major cerebral artery blockage.

To the authors knowledge, the only available infarct volume estimation based on simulations was 238 [ml] [12] before the current study. The results demonstrate that perfusion simulations with inferred parameters can explain a significant part of the clinically measured infarct volume distribution. However, a substantial part of the infarct volume distribution remains poorly understood. The aforementioned findings indicate that structural and perfusion-weighted MRI data alongside blood pressure measurements are necessary but not sufficient for patient-specific perfusion simulations.

Simulated infarct volumes are estimated based on absolute or relative perfusion thresholds. Infarct estimation using relative perfusion threshold is known to overestimate the ischaemic region compared to diffusion-weighted MRI [65]. By comparison, the absolute perfusion threshold resulted in a larger than 5 [ml] volume labelled as infarct in 3 out of 75 healthy simulations.

5.3. Limitations

This study has several limitations. Firstly, the affine transformation of the mesh template keeps the volume ratios of various tissue regions constant. Therefore, variations in grey and white matter volume ratios cannot be captured by the proposed automated parameter inference approach. It requires further investigations to evaluate whether a non-linear mesh transformation would be suitable to capture more subtle anatomical details and thus achieve better anatomical fitness. For example, the current framework based on linear mesh transformation cannot account for variations in the volume fraction of tissue regions and the shape of CSF spaces which might be caused by brain atrophy.

Secondly, many physiological parameters were not included in this model for the sake of simplicity. Such parameters include the intracranial pressure and the arterial pressure which probably differ significantly in healthy cohorts and AIS patients [66]. However, experimental data are scarce and other crucial model parameters might be even more challenging to determine. For example, the vector space aligned with the centrelines of descending arterioles is necessary to compute the permeability tensor $\boldsymbol{K}$ representing the conductance of penetrating arterioles. However, experimental techniques have not yet been proposed to determine the aforementioned vector space or the $\boldsymbol{K}$ field.

Thirdly, the test case regarding occluded scenarios emphasises the importance of crucial compensatory mechanisms, e.g., collateralisation [2,63], which lowers the chance of infarct formation. Future studies should aim to incorporate such effects into computational models as proposed in [67,68]. Without such details, simulations cover solely the 'right tail' of the infarct volume distribution representing the largest infarcts. Furthermore, it is important to add processes which can be responsible for the lack of reperfusion after recanalisation, such as pericyte constriction [69] and microembolism [11,70] to account for treatment effects.

Fourthly, the utilised model accounts only for a part of the circulation stretching from the descending arterioles to the ascending venules of the brain. It is important to acknowledge that the region of interest of this study is in strong interaction with other parts of the circulation. However, upstream and downstream effects including the heart and the veins are lumped solely into the imposed average perfusion pressure. Such simplifications become questionable in diseased scenarios. For example, oedema after AIS can result in local perfusion pressure drop [71] which the heart might compensate with increased cardiac output. Such complex cases could be modelled by integrating preclinical and clinical data into multiple coupled models covering the extended region of interest.

Finally, the utilised perfusion model accounts solely for the space-dependence of brain perfusion. Previously, it has been proposed that cerebral autoregulation [66] is impaired in AIS patients and spreading depolarisation promotes infarct formation [72]. Therefore, perfusion in AIS patients is likely impacted by vascular changes and neurovascular coupling in the vicinity of the spreading infarcted region. The interplay of such spatiotemporal vascular, neural, metabolic, and haemodynamic processes remains unexplored primarily because of extreme difficulties associated with relevant quantitative data acquisition, especially in humans. The present modelling framework does not incorporate the aforementioned effects, but it does provide a solid foundation to facilitate future extensions in cohort-level perfusion simulations.

6. Conclusions

The proposed parameter inference approach integrates human neuroimaging data to estimate anatomical (geometrical) and haemodynamic model parameters, and thus reach the goal of the present study regarding the realisation of cohort-level perfusion simulations. The present study reports overall 225 brain simulations including 75 healthy cases, and 150 ischaemic stroke cases with 75 left and 75 right middle cerebral artery occlusions. Group-level tissue volume and cerebral blood flow measurements in the model brains match clinical observations corresponding to the healthy reference cohort used for model parameter tuning. Furthermore, simulations provided qualitatively and quantitatively realistic predictions regarding the infarct location and size in cohorts of AIS patients.

The present study demonstrates how cerebral perfusion simulations can integrate existing knowledge from various sources, including pre-clinical and clinical investigations. The results further computational perfusion modelling as a novel tool to boost medical device and drug development by breaking previous barriers associated with small sample size.

CRediT authorship contribution statement

T.I. Józsa: Conceptualisation, Carrying out research, performing image processing, Developing mathematical and computational models, writing the manuscript under the supervision of JP, SJP, and HJMMM. **J. Petr:** Supervision of image processing activities and data analysis, Writing of the manuscript. **S.J. Payne:** Supervision of mathematical and computational model development, Funding Acquisition, Writing of the manuscript. **H.J.M.M. Mutsaerts:** Supervision of clinical data processing and image processing activities, Funding acquisition, Writing of the manuscript.

Declaration of competing interest

The authors declare that they do not have conflicting interests.

Acknowledgements

This research, and TIJ in particular, was supported by the Amsterdam UMC Postdoc Career Bridging Grant and the European Union's Horizon 2020 research and innovation program (Grant No. 777072, INSIST project). SJP was supported by a Yushan Fellowship from the Ministry of Education, Taiwan (#111V1004-2). HJMMM was supported by the Dutch Heart Foundation (03-004-2020T049), and by the Eurostars-2 joint program with co-funding from the European Union Horizon 2020 research and innovation program, provided by the Netherlands Enterprise Agency (RvO). The EPAD data were obtained with support from the following EU/EFPIA Innovative Medicines Initiatives (1 and 2) Joint Undertakings: EPAD (Grant No. 115736), AMYPAD (Grant No. 115952). The authors are grateful to the members of the INSIST consortium for valuable discussions and their sustained support and thank Giulia Luraghi of the Politecnico di Milano and Kevin Moerman of National University of Ireland Galway for the valuable discussions on brain mesh generation.

Appendix. Alternative cerebral perfusion pressure estimation

Cerebral perfusion pressure (CPP) is often estimated as the difference between mean arterial pressure (MAP) and intracranial pressure (ICP) [73] so that

$$\mathrm{CPP} = \mathrm{MAP} - \mathrm{ICP}. \tag{11}$$

An approximate formula [74] for the MAP based on diastolic (DBP) and systolic (SBP) blood pressure measurement is

$$\mathrm{MAP} = \mathrm{SBP} + \frac{\mathrm{SBP} - \mathrm{DBP}}{3}. \tag{12}$$

Normotension is associated with MAP $\leq$ 90 mmHg [74]. By comparison, the average MAP in stroke patient cohorts can exceed 110 mmHg [26].

ICP monitoring relies on invasive techniques and therefore human experimental data remain scarce. ICP in healthy adults lying in supine position has been estimated to range between 0.5 and 15 mmHg [73,75]. The corresponding expected CPP value in healthy adults might fall below 65 mmHg whereas in stroke patients it might reach 110 mmHg.

The present study considers cohorts of male and female reference subjects with a relatively wide age range to simulate perfusion under healthy circumstances and in AIS. Due to the lack of ICP data in untreated AIS patients, it is assumed that the CPP distributions in the healthy and the stroke cohorts are identical. The utilised CPP values are sampled from a normal distribution with a mean value of 85 mmHg and a standard deviation of 10 mmHg resulting in an $[\approx 60;\ \approx 108]$ mmHg range and quartiles of ≈78, ≈86, and ≈91 mmHg. The sampled CPP are considered realistic based on Eqs. (11) and (12), and the publicly available MAP and ICP data.

References

[1] P.S.S. Fransen, D. Beumer, O.A. Berkhemer, L.A. van den Berg, H. Lingsma, A. van der Lugt, W.H. van Zwam, R.J. van Oostenbrugge, Y.B.W.E.M. Roos, C.B. Majoie, et al., MR CLEAN, a multicenter randomized clinical trial of endovascular treatment for acute ischemic stroke in the netherlands: study protocol for a randomized controlled trial, Trials 15 (1) (2014) 343.

[2] D.S. Liebeskind, Reperfusion for acute ischemic stroke: arterial revascularization and collateral therapeutics, Curr. Opin. Neurol. 23 (1) (2010) 36–45.

[3] O.A. Berkhemer, P.S.S. Fransen, D. Beumer, L.A. van den Berg, H.F. Lingsma, A.J. Yoo, W.J. Schonewille, J.A. Vos, P.J. Nederkoorn, M.J.H. Wermer, et al., A randomized trial of intraarterial treatment for acute ischemic stroke, N. Engl. J. Med. 372 (1) (2015) 11–20.

[4] M. Goyal, B.K. Menon, W.H. van Zwam, D.W.J. Dippel, P.J. Mitchell, A.M. Demchuk, A. Dávalos, C.B.L.M. Majoie, A. Van Der Lugt, M.A. De Miquel, et al., Endovascular thrombectomy after large-vessel ischaemic stroke: a meta-analysis of individual patient data from five randomised trials, Lancet 387 (10029) (2016) 1723–1731.

[5] P.R. Konduri, H.A. Marquering, E.E. van Bavel, A. Hoekstra, C.B.L.M. Majoie, the INSIST Investigators, In-silico trials for treatment of acute ischemic stroke, Front. Neurol. 11 (2020) 1062.

[6] C. Miller, R.M. Padmos, M. van der Kolk, T.I. Józsa, N. Samuels, Y. Xue, S.J. Payne, A.G. Hoekstra, In silico trials for treatment of acute ischemic stroke: Design and implementation, Comput. Biol. Med. 137 (2021) 104802.

[7] R. Petkantchin, R. Padmos, K.Z. Boudjeltia, F. Raynaud, B. Chopard, et al., Thrombolysis: Observations and numerical models, J. Biomech. (2021) 110902.

[8] P.H. Mangin, K.B. Neeves, W.A. Lam, J.M.E.M. Cosemans, N. Korin, S.W. K., M.A. Panteleev, S. on Biorheology, In vitro flow-based assay: From simple toward more sophisticated models for mimicking hemostasis and thrombosis, J. Thromb. Haemost. 19 (2) (2021) 582–587.

[9] G. Luraghi, J.F. Rodriguez-Matas, G. Dubini, F. Berti, S. Bridio, S. Duffy, A. Dwivedi, R. McCarthy, B. Fereidoonnezhad, P. McGarry, et al., Applicability assessment of a stent-retriever thrombectomy finite-element model, Interface Focus 11 (1) (2021) 20190123.

[10] K.M. Moerman, P. Konduri, B. Fereidoonnezhad, H. Marquering, A. van der Lugt, G. Luraghi, S. Bridio, F. Migliavacca, J.F.R. Matas, P. McGarry, Development of a patient-specific cerebral vasculature fluid-structure-interaction model, J. Biomech. (2022) 110896.

[11] W.K. El-Bouri, A. MacGowan, T.I. Józsa, M.J. Gounis, S.J. Payne, Modelling the impact of clot fragmentation on the microcirculation after thrombectomy, PLoS Comput. Biol. 17 (3) (2021) e1008515.

[12] T.I. Józsa, R.M. Padmos, N. Samuels, W.K. El-Bouri, A.G. Hoekstra, S.J. Payne, A porous circulation model of the human brain for in silico clinical trials in ischaemic stroke, Interface Focus 11 (1) (2021) 20190127.

[13] T.I. Józsa, R.M. Padmos, W.K. El-Bouri, A.G. Hoekstra, S.J. Payne, On the sensitivity analysis of porous finite element models for cerebral perfusion estimation, Ann. Biomed. Eng. 49 (12) (2021) 3647–3665.

[14] E. Hodneland, E. Hanson, O. Sævareid, G. Nævdal, A. Lundervold, V. Šoltészová, A.Z. Munthe-Kaas, A. Deistung, J.R. Reichenbach, J.M. Nordbotten, A new framework for assessing subject-specific whole brain circulation and perfusion using MRI-based measurements and a multi-scale continuous flow model, PLoS Comput. Biol. 15 (6) (2019) e1007073.

[15] B. Tully, Y. Ventikos, Cerebral water transport using multiple-network poroelastic theory: application to normal pressure hydrocephalus, J. Fluid Mech. 667 (2011) 188–215.

[16] L. Guo, Z. Li, J. Lyu, Y. Mei, J.C. Vardakis, D. Chen, C. Han, X. Lou, Y. Ventikos, On the validation of a multiple-network poroelastic model using arterial spin labeling MRI data, Front. Comput. Neurosci. 13 (2019) 60.

[17] Y. Huang, L.C. Parra, S. Haufe, The New York Head–A precise standardized volume conductor model for EEG source localization and tES targeting, NeuroImage 140 (2016) 150–162.

[18] A.P. Tran, S. Yan, Q. Fang, Improving model-based functional near-infrared spectroscopy analysis using mesh-based anatomical and light-transport models, Neurophotonics 7 (1) (2020) 015008.

[19] W.K. El-Bouri, S.J. Payne, Multi-scale homogenization of blood flow in 3-dimensional human cerebral microvascular networks, J. Theoret. Biol. 380 (2015) 40–47.

[20] A.F. Smith, V. Doyeux, M. Berg, M. Peyrounette, M. Haft-Javaherian, A.-E. Larue, J.H. Slater, F. Lauwers, P. Blinder, P. Tsai, D. Kleinfeld, C.B. Schaffer, N. Nishimura, Y. Davit, S. Lorthois, Brain capillary networks across species: a few simple organizational requirements are sufficient to reproduce both structure and function, Front. Physiol. 10 (2019) 233.

[21] A.R. Pries, T.W. Secomb, T. Gessner, M.B. Sperandio, J.F. Gross, P. Gaehtgens, Resistance to blood flow in microvessels in vivo, Circ. Res. 75 (5) (1994) 904–915.

[22] A.S. Dekaban, D. Sadowsky, Changes in brain weights during the span of human life: relation of brain weights to body heights and body weights, Ann. Neurol. 4 (4) (1978) 345–356.

[23] E. Lüders, H. Steinmetz, L. Jäncke, Brain size and grey matter volume in the healthy human brain, Neuroreport 13 (17) (2002) 2371–2374.

[24] P.A. Hasgall, F. Di Gennaro, C. Baumgartner, E. Neufeld, B. Lloyd, M.C. Gosselin, D. Payne, A. Klingenböck, N. Kuster, IT'IS Database for thermal and electromagnetic parameters of biological tissues, 2018, http://dx.doi.org/10.13099/VIP21000-04-0.

[25] F. Cassot, F. Lauwers, C. Fouard, S. Prohaska, V. Lauwers-Cances, A novel three-dimensional computer-assisted method for a quantitative study of microvascular networks of the human cerebral cortex, Microcirculation 13 (1) (2006) 1–18.

[26] K. Malhotra, N. Ahmed, A. Filippatou, A.H. Katsanos, N. Goyal, K. Tsioufis, E. Manios, M. Pikilidou, P.D. Schellinger, A.W. Alexandrov, et al., Association of elevated blood pressure levels with outcomes in acute ischemic stroke patients treated with intravenous thrombolysis: a systematic review and meta-analysis, J. Stroke 21 (1) (2019) 78.

[27] A.H. Werber, D.D. Heistad, Effects of chronic hypertension and sympathetic nerves on the cerebral microvasculature of stroke-prone spontaneously hypertensive rats, Circ. Res. 55 (3) (1984) 286–294.

[28] L. Tatu, T. Moulin, J. Bogousslavsky, H. Duvernoy, Arterial territories of the human brain: cerebral hemispheres, Neurology 50 (6) (1998) 1699–1708.

[29] C.W. Ritchie, J.L. Molinuevo, L. Truyen, A. Satlin, S. Van der Geyten, S. Lovestone, et al., Development of interventions for the secondary prevention of Alzheimer's dementia: the European Prevention of Alzheimer's Dementia (EPAD) project, The Lancet Psychiatry 3 (2) (2016) 179–186.

[30] H.J.M.M. Mutsaerts, et al., ExploreASL: an image processing pipeline for multi-center ASL perfusion MRI studies, NeuroImage 219 (2020) 117031.

[31] C. Gaser, Partial volume segmentation with adaptive maximum a posteriori (MAP) approach, NeuroImage 47 (2009) S121.

[32] IXI dataset, 2023. https://brain-development.org/ixi-dataset/. (Accessed 06 February 2023).

[33] I. Asllani, A. Borogovac, T.R. Brown, Regression algorithm correcting for partial volume effects in arterial spin labeling MRI, Magn. Reson. Med. 60 (6) (2008) 1362–1371.

[34] D.C. Alsop, J.A. Detre, X. Golay, M. Günther, J. Hendrikse, L. Hernandez-Garcia, H. Lu, B.J. MacIntosh, L.M. Parkes, M. Smits, et al., Recommended implementation of arterial spin-labeled perfusion MRI for clinical applications: a consensus of the ISMRM perfusion study group and the European consortium for ASL in dementia, Magn. Reson. Med. 73 (1) (2015) 102–116.

[35] R. Oostenveld, P. Fries, E. Maris, J.-M. Schoffelen, FieldTrip: open source software for advanced analysis of MEG, EEG, and invasive electrophysiological data, Comput. Intell. Neurosci. (2011) 156869.

[36] J.D. Nielsen, K.H. Madsen, O. Puonti, H.R. Siebner, C. Bauer, C.G. Madsen, G.B. Saturnino, A. Thielscher, Automatic skull segmentation from MR images for realistic volume conductor models of the head: Assessment of the state-of-the-art, NeuroImage 174 (2018) 587–598.

[37] R. Dahnke, R.A. Yotter, C. Gaser, Cortical thickness and central surface estimation, NeuroImage 65 (2013) 336–348.

[38] C. Hutton, E. De Vita, J. Ashburner, R. Deichmann, R. Turner, Voxel-based cortical thickness measurements in MRI, NeuroImage 40 (4) (2008) 1701–1710.

[39] A. Adam, Mesh voxelisation, 2022, www.mathworks.com/matlabcentral/fileexchange/27390-mesh-voxelisation, MATLAB Central File Exchange. Retrieved 3 March 2022.

[40] M.A. Chappell, F.A.K. McConnell, X. Golay, M. Günther, J.A. Hernandez-Tamames, M.J. van Osch, I. Asllani, Partial volume correction in arterial spin labeling perfusion MRI: A method to disentangle anatomy from physiology or an analysis step too far? Neuroimage 238 (2021) 118236.

[41] M. Jenkinson, P. Bannister, M. Brady, S. Smith, Improved optimization for the robust and accurate linear registration and motion correction of brain images, NeuroImage 17 (2) (2002) 825–841.

[42] M. Jenkinson, C.F. Beckmann, T.E.J. Behrens, M.W. Woolrich, S.M. Smith, FSL, NeuroImage 62 (2) (2012) 782–790.

[43] A.M.M. Boers, I.G.H. Jansen, S. Brown, H.F. Lingsma, L.F.M. Beenen, T.G. Devlin, L. San Román, J.-H. Heo, M. Ribó, M.A. Almekhlafi, et al., Mediation of the relationship between endovascular therapy and functional outcome by follow-up infarct volume in patients with acute ischemic stroke, JAMA Neurol. 76 (2) (2019) 194–202.

[44] T.G. Jovin, J.L. Saver, M. Ribo, V. Pereira, A. Furlan, A. Bonafe, B. Baxter, R. Gupta, D. Lopes, O. Jansen, W. Smith, D. Gress, S. Hetts, R.J. Lewis, R. Shields, S.M. Berry, T.L. Graves, T. Malisch, A. Rai, K.N. Sheth, D.S. Liebeskind, R.G. Nogueira, Diffusion-weighted imaging or computerized tomography perfusion assessment with clinical mismatch in the triage of wake up and late presenting strokes undergoing neurointervention with Trevo (DAWN) trial methods, Int. J. Stroke 12 (6) (2017) 641–652.

[45] A.C. Pereira, D.E. Saunders, V.L. Doyle, J.M. Bland, F.A. Howe, J.R. Griffiths, M.M. Brown, Measurement of initial N-acetyl aspartate concentration by magnetic resonance spectroscopy and initial infarct volume by MRI predicts outcome in patients with middle cerebral artery territory infarction, Stroke 30 (8) (1999) 1577–1582.

[46] A.M. Boers, H.A. Marquering, J.J. Jochem, N.J. Besselink, O.A. Berkhemer, A. van der Lugt, L.F. Beenen, C.B. Majoie, Automated cerebral infarct volume measurement in follow-up noncontrast CT scans of patients with acute ischemic stroke, Amer. J. Neuroradiol. 34 (8) (2013) 1522–1527.

[47] A. Logg, G.N. Wells, DOLFIN: Automated finite element computing, ACM Trans. Math. Software 37 (2) (2010) 1–28.

[48] P. Virtanen, R. Gommers, T.E. Oliphant, M. Haberland, T. Reddy, D. Cournapeau, E. Burovski, P. Peterson, W. Weckesser, J. Bright, S.J. van der Walt, M. Brett, J. Wilson, K.J. Millman, N. Mayorov, A.R.J. Nelson, E. Jones, R. Kern, E. Larson, C.J. Carey, İ. Polat, Y. Feng, E.W. Moore, J. Van der Plas, D. Laxalde, J. Perktold, R. Cimrman, I. Henriksen, E.A. Quintero, C.R. Harris, A.M. Archibald, A.H. Ribeiro, F. Pedregosa, P. van Mulbregt, SciPy 1.0 Contributors, SciPy 1.0: Fundamental algorithms for scientific computing in python, Nature Methods 17 (2020) 261–272.

[49] M.A. Ikram, H.A. Vrooman, M.W. Vernooij, F. van der Lijn, A. Hofman, A. van der Lugt, W.J. Niessen, M.M.B. Breteler, Brain tissue volumes in the general elderly population: The Rotterdam Scan Study, Neurobiol. Aging 29 (6) (2008) 882–890.

[50] A.M. Winkler, M.R. Sabuncu, B.T.T. Yeo, B. Fischl, D.N. Greve, P. Kochunov, T.E. Nichols, J. Blangero, D.C. Glahn, Measuring and comparing brain cortical surface area and other areal quantities, NeuroImage 61 (4) (2012) 1428–1443.

[51] L. Zarrinkoob, K. Ambarki, A. Wåhlin, R. Birgander, A. Eklund, J. Malm, Blood flow distribution in cerebral arteries, J. Cereb. Blood Flow Metab. 35 (4) (2015) 648–654.

[52] C.-Y. Xing, T. Tarumi, J. Liu, Y. Zhang, M. Turner, J. Riley, C.D. Tinajero, L.-J. Yuan, R. Zhang, Distribution of cardiac output to the brain across the adult lifespan, J. Cereb. Blood Flow Metab. 37 (8) (2017) 2848–2856.

[53] A.C. Van Loenhoud, C. Groot, D.I. Bocancea, F. Barkhof, C. Teunissen, P. Scheltens, W.M. Van De Flier, R. Ossenkoppele, Association of education and intracranial volume with cognitive trajectories and mortality rates across the Alzheimer disease continuum, Neurology 98 (16) (2022) e1679–e1691.

[54] D.F.R. Heijtel, H.J.M.M. Mutsaerts, E. Bakker, P. Schober, M.F. Stevens, E.T. Petersen, B.N.M. van Berckel, C.B.L.M. Majoie, J. Booij, M.J.P. van Osch, E. van Bavel, R. Boellaard, A.A. Lammertsma, A.J. Nederveen, Accuracy and precision of pseudo-continuous arterial spin labeling perfusion during baseline and hypercapnia: a head-to-head comparison with ^{15}O H2O positron emission tomography, NeuroImage 92 (2014) 182–192.

[55] L. Guo, J.C. Vardakis, T. Lassila, M. Mitolo, N. Ravikumar, D. Chou, M. Lange, A. Sarrami-Foroushani, B.J. Tully, Z.A. Taylor, S. Varma, A. Venneri, A.J. Frangi, Y. Ventikos, Subject-specific multi-poroelastic model for exploring the risk factors associated with the early stages of Alzheimer's disease, Interface Focus 8 (1) (2018) 20170019.

[56] L. Guo, J.C. Vardakis, D. Chou, Y. Ventikos, A multiple-network poroelastic model for biological systems and application to subject-specific modelling of cerebral fluid transport, Internat. J. Engrg. Sci. 147 (2020) 103204.

[57] K.-A. Mardal, M.E. Rognes, T.B. Thompson, L.M. Valnes, Mathematical Modeling of the Human Brain – From Magnetic Resonance Images to Finite Element Simulation, Springer, 2022.

[58] B. Fischl, FreeSurfer, NeuroImage 62 (2) (2012) 774–781.

[59] Y. Zhang, M. Brady, S. Smith, Segmentation of brain MR images through a hidden Markov random field model and the expectation-maximization algorithm, IEEE Trans. Med. Imaging 20 (1) (2001) 45–57.

[60] W.D. Penny, K.J. Friston, J.T. Ashburner, S.J. Kiebel, T.E. Nichols, Statistical Parametric Mapping: the Analysis of Functional Brain Images, Elsevier, 2011.

[61] D. Garcia-Gonzalez, J. Jayamohan, S.N. Sotiropoulos, S.-H. Yoon, J. Cook, C.R. Siviour, A. Arias, A. Jérusalem, On the mechanical behaviour of PEEK and HA cranial implants under impact loading, J. Mech. Behav. Biomed. Mater. 69 (2017) 342–354.

[62] H.J.M.M. Mutsaerts, J.W. van Dalen, D.F.R. Heijtel, P.F.C. Groot, C.B.L.M. Majoie, E.T. Petersen, E. Richard, A.J. Nederveen, Cerebral perfusion measurements in elderly with hypertension using arterial spin labeling, PLoS One 10 (8) (2015) e0133717.

[63] A.M.M. Boers, R.S. Barros, I.G.H. Jansen, O.A. Berkhemer, L.F.M. Beenen, B.K. Menon, D.W.J. Dippel, A. van der Lugt, W.H. van Zwam, Y.B.W.E.M. Roos, et al., Value of quantitative collateral scoring on CT angiography in patients with acute ischemic stroke, Amer. J. Neuroradiol. 39 (6) (2018) 1074–1082.

[64] S.J. Payne, Cerebral Blood Flow and Metabolism: A Quantitative Approach, World Scientific, 2017.

[65] W.A. Copen, A.J. Yoo, N.S. Rost, L.T. Morais, P.W. Schaefer, R.G. Gonzalez, O. Wu, In patients with suspected acute stroke, CT perfusion-based cerebral blood flow maps cannot substitute for DWI in measuring the ischemic core, PLoS One 12 (11) (2017).

[66] P.J. Eames, M.J. Blake, S.L. Dawson, R.B. Panerai, J.F. Potter, Dynamic cerebral autoregulation and beat to beat blood pressure control are impaired in acute ischaemic stroke, J. Neurol. Neurosurg. Psychiatry 72 (4) (2002) 467–472.

[67] R.M. Padmos, T.I. Józsa, W.K. El-Bouri, P.R. Konduri, S.J. Payne, A.G. Hoekstra, Coupling one-dimensional arterial blood flow to three-dimensional tissue perfusion models for in silico trials of acute ischaemic stroke, Interface Focus 11 (1) (2021) 20190125.

[68] R.M. Padmos, N.A. Terreros, T.I. Józsa, G. Závodszky, H.A. Marquering, C.B.L.M. Majoie, A.G. Hoekstra, Modelling the leptomeningeal collateral circulation during acute ischaemic stroke, Med. Eng. Phys. 91 (2021) 1–11.

[69] D. Attwell, A. Mishra, C.N. Hall, F.M. O'Farrell, T. Dalkara, What is a pericyte? J. Cereb. Blood Flow Metab. 36 (2) (2016) 451–455.

[70] Y. Xue, W.K. El-Bouri, T.I. Józsa, S.J. Payne, Modelling the effects of cerebral microthrombi on tissue oxygenation and cell death, J. Biomech. 127 (2021) 110705.
[71] X. Chen, T.I. Józsa, S.J. Payne, Computational modelling of cerebral oedema and osmotherapy following ischaemic stroke, Comput. Biol. Med. 151 (2022) 106226.
[72] C. Dohmen, O.W. Sakowitz, M. Fabricius, B. Bosche, T. Reithmeier, R.-I. Ernestus, G. Brinker, J.P. Dreier, J. Woitzik, A.J. Strong, et al., Spreading depolarizations occur in human ischemic stroke with high incidence, Ann. Neurol. 63 (6) (2008) 720–728.
[73] L.A. Steiner, P.J.D. Andrews, Monitoring the injured brain: ICP and CBF, Br. J. Anaesthesia 97 (1) (2006) 26–38.
[74] J.D. Melgarejo, W.-Y. Yang, L. Thijs, Y. Li, K. Asayama, T.W. Hansen, M. Wei, T. Ohkubo, E. Dolan, K. Stolarz-Skrzypek, Q.-F. Huang, V. Tikhonoff, S. Malyutina, E. Casiglia, L. Lind, E. Sandoya, J. Filipovský, N. Gilis-Malinowska, K. Narkiewicz, K. Kawecka-Jaszcz, J. Boggia, J.-G. Wang, Y. Imai, T. Vanassche, P. Verhamme, S. Janssens, E. O'Brien, G.E. Maestre, J.A. Staessen, Z.-Y. Zhang, Association of fatal and nonfatal cardiovascular outcomes with 24-hour mean arterial pressure, Hypertension 77 (1) (2021) 39–48.
[75] M. Andresen, M. Juhler, Intracranial pressure following complete removal of a small demarcated brain tumor: a model for normal intracranial pressure in humans, J. Neurosurgery 121 (4) (2014) 797–801.



https://dspace.org/

MRI-based parameter inference for cerebral perfusion modelling in health and ischaemic stroke

Józsa, Tamás I.; Petr, Jan; Payne, Stephen J.; Mutsaerts, Henk J. M. M.

2023-11-01
Elsevier
https://doi.org/10.1016/j.compbiomed.2023.107543
Józsa TI, Petr J, Payne SJ, Mutsaerts HJMM. (2023) MRI-based parameter inference for cerebral perfusion modelling in health and ischaemic stroke. Computers in Biology and Medicine, Volume 166, November 2023, Article Number 107543

Downloaded from a DSpace repository. https://dspace.org/